

Spectral Variability of the Uranyl Silicates Uranophane-alpha and Uranophane-beta: Polymorphism and Luminescence

Martin Stark (✉ martin.stark@gmx.org)

Markus Noller

Research Article

Keywords: Spectroscopy, luminescence, uranophane, polymorphism, uranium minerals

Posted Date: June 14th, 2022

DOI: <https://doi.org/10.21203/rs.3.rs-1735853/v1>

License: © ⓘ This work is licensed under a Creative Commons Attribution 4.0 International License.

[Read Full License](#)

Abstract

The luminescence of the uranyl cation UO_2^{2+} depends on the local crystalline environment and is sensitive to structural influences. Luminescence spectra of the related uranyl silicates uranophane- α , uranophane- β , sklodowskite and haiweeite from various locations are presented and discussed in the light of structure-property relation. The four mineral species were chosen for their close relationships: uranophane- α and uranophane- β are polymorphs and share the underlying topology with sklodowskite. Haiweeite, of different topology, shares the composing elements Ca, U, Si, O with uranophane, while in sklodowskite Mg replaces Ca. All species show some variability in their spectra, parameterized as variation of centroid wavelength. Importantly, a prominent – partly dominating – double peak-structure occurs in the case of uranophane- α only, while it is absent in the spectra of the other species. Considering a model of luminescent transitions in the uranyl-ion in more detail, this observation is discussed in the light of the polymorphism of uranophane. We show evidence that variable amounts of uranophane- β phase embedded in uranophane- α are possibly at the origin of this spectral signature. Growth of those uranophane- β clusters might be induced by defects in the uranophane- α lattice and further promoted by the polymorphism of uranophane.

1 Introduction

In many crystalline environments the uranyl-cation UO_2^{2+} exhibits a characteristic greenish to yellow luminescence with spectroscopic properties mostly related to the molecular character of uranyl-luminescence (Fron del 1958; Blasse 1987; Gorobets 2002). The characteristic features of excitation and emission spectra depend on the local environment of the uranyl ion defined by ligands or the crystalline matrix (Blasse 1987; Görrler-Walrand et al. 2004; Pierloot and van Besien 2005; Drobot 2015a; Višňák and Sobek 2016; Haubitz et al. 2018). With additional ligands in solution, the uranyl-ion UO_2^{2+} can form more complex ions like e.g. UO_2OH^+ , $(\text{UO}_2)_3(\text{OH})^{7-}$ or $\text{UO}_2(\text{CO}_3)_3^{4-}$, depending on environmental conditions (as e.g. temperature, pH) and available ligands (Moulin et al. 1998, Mühr-Ebert et al. 2019, Romanchuck et al. 2020).

This speciation connects chemically driven alteration processes to environmentally relevant migration processes in specific geological settings. Soluble uranium ions migrate in the environment and might eventually interfere with human activities, e.g. contaminating water resources or being enriched in the food chain. For remediation of possibly contaminated areas, but as well for environmental monitoring in the context of storage of spent nuclear fuel, insight in speciation processes is a key issue. Luminescence spectroscopy proved to be a valuable tool for characterizing uranyl speciation (Meinrath 1997; Moulin et al. 1998, Collins et al. 2011, Drobot et al. 2015b). Further methodology has been proposed for environmental monitoring in the context of waste management and remediation of possibly contaminated sites (e.g. DeNeufville et al. 1981; Meinrath et al. 2003; Nelson 2009; Arnold et al. 2011; Frankland et al. 2021).

The migration of uranyl ions in liquid environment is among others influenced by sorption processes and the initiation of crystal growth. Mobile uranium species are transformed into (meta-) stable forms, e.g. as mineral coatings or crystalline components of soil. Local growth of crystals removes uranyl ions from solution, thus limiting migration (Wronkiewicz et al. 1996). However, dust formed subsequently by mechanical erosion is again subject to transport by wind or, in technical systems, by airflow and ventilation. Similar to the case in solution, the luminescence is characteristic for the mineral species involved. Spectra of uranium-bearing minerals have been explored as additional information to identify mineral species (Haberlandt et al. 1950; Gorobets 2002) and as well to monitor environmental issues (Cunnane et al. 1993; Geipel et al. 2000; Wang et al. 2005; Massuyeau et al. 2017).

At this point, it is of interest to examine spectral variability and its relation to structure as well as structural disorder. Such insight is not only relevant to estimate reliability of spectroscopic screening data, e.g. for environmental monitoring, but as well to address structure-property relations. As the luminescence of the cation UO_2^{2+} is sensitive to its local environment, UO_2^{2+} can be conceived as local probe to explore structural variability. Information gained by luminescence spectroscopy relies on an ensemble of target units (ions or groups acting as luminescent centers) which is different from the target units addressed by x-ray diffraction (XRD, electron densities) or Raman spectroscopy (polarizable chemical bonds and their vibrational modes). Therefore, luminescence spectroscopy provides information complementary to that provided by XRD or Raman.

Table 1
Relevant properties of the minerals in this study

Mineral name	Composition	Space group	Characteristic structural element ^a	References
Uranophane- α	$\text{Ca}(\text{UO}_2)_2(\text{SiO}_3\text{OH})_2 \cdot 5\text{H}_2\text{O}$	$P2_1$...ud...	Ginderow 1988; Cesbron et al. 1993; Burns 2005; Colmenero et al. 2018; Plášil 2018a
Uranophane- β	$\text{Ca}(\text{UO}_2)_2(\text{SiO}_3\text{OH})_2 \cdot 5\text{H}_2\text{O}$	$P2_1/c$...uudd...	Viswanathan et al. 1986; Plášil 2018a ; Plášil 2018b ; Colmenero et al. 2019
Sklodowskite	$\text{Mg}(\text{UO}_2)_2(\text{SiO}_3\text{OH})_2 \cdot 6\text{H}_2\text{O}$	$C2/m$...ud...	Burns 2005, Plášil 2018a
Haiweeite	$\text{Ca}(\text{UO}_2)_2(\text{Si}_5\text{O}_{12})(\text{OH})_2 \cdot 6\text{H}_2\text{O}$	$Pbcn$	not applicable	Burns 2001, Plášil et al. 2013
^a see details in the text and in Plášil 2018a				

Here, we address the spectral variability of the natural uranyl-silicates uranophane- α , uranophane- β , sklodowskite, and haiweeite. Uranyl silicates are relevant in the context of uranium-migration, as they represent common and rather stable alteration products (Wronkiewicz et al. 1996). These uranyl-silicates

form aggregates of similar appearance (see Fig. 1) and are closely related in chemistry and structure (Table 1).

Main focus is directed towards the polymorphism of uranophane and its influence on spectroscopic properties, with the two other species providing a reference frame. Sklodowskite shares main structural elements with uranophane- α and is chemically closely related to uranophane with Mg replacing Ca. Especially, no polymorph is known for sklodowskite. Haiweeite on the other hand shares the constituting chemical elements with uranophane, but exhibits a distinctly different structure.

Further motivation to focus closer on spectral variability arises from observations shown in Fig. 2. There, spectra of three uranophane- α crystals (#089/3, Musonoi, DR Congo; #017, Rauris, Austria; #012, Le Limouzat, France; for all of them, identity was confirmed by XRD and EDS) are given (Fig. 2a), highlighting a remarkable spectral variability. While in #089/3, the clear phononic sequence is built up by single emission peaks, a pronounced double peak structure is visible in #017, similar to that presented by Kuta and colleagues (2013) – there, notably measured on synthetic material. Eventually, spectrum #012 is broadened and starts losing structure. The photograph in Fig. 2b shows two aggregates of uranophane- α extracted from different samples from Menzenschwand, Germany, luminescing under ultraviolet excitation. The difference in luminescence color is clearly visible.

In this study we show important spectral variability especially in the case of uranophane- α , and propose local structural variability related to the polymorphism of uranophane as possible origin. The outline of the article is as follows:

The structure of the uranyl-silicates under focus, their luminescence mechanism and the interplay between structure and luminescence are briefly outlined. Luminescence spectra and spectral variability of (in total) more than 80 samples from about 30 different localities have been investigated and analyzed. Especially, localization of spectral fluctuations is demonstrated by spatially resolved measurements on individual crystals. Based on these findings, we discuss evidence for enhanced spectral variability of uranophane- α as compared to its counterpart uranophane- β and to the other species, sklodowskite and haiweeite. Results are related to local structural variability and polymorphism, which possibly is at the origin of the observed spectral fluctuations.

2 Structure And Luminescence

2.1 Structural elements of uranophane- α , uranophane- β , sklodowskite and haiweeite

First, we consider structural elements relevant to spectral variability, for details we refer the reader to the given literature. The structures of both uranophane polymorphs have been investigated intensely, either uranophane- α (Ginderow 1988; Barinova et al. 2001; Colmenero et al., 2018) and uranophane- β (Viswanathan et al. 1986; Barinova et al. 2003; Colmenero et al. 2019) separately, or in comparison and

together with other uranium-bearing minerals (Stohl et al. 1981; Cesbron et al. 1993; Burns et al. 1996; Burns 2005; Plášil 2018a). Both polymorphs base on a sheet structure, where uranophane- α belongs to spacegroup $P2_1$ and uranophane- β to $P2_1/c$. Despite different symmetry, they base on equivalent topology, the *uranophane topology* (Burns 2005; Plášil 2018a). Main structural elements are (UO_7) -pentagonal bipyramids and $[\text{SiO}_3(\text{OH})]$ -groups, with the (UO_7) -bipyramids connected by edges to form chains. These chains are interconnected by SiO_4 -tetrahedra (Fig. 3a, b). To highlight the chain-tetrahedra motives, only (UO_7) -bipyramids (yellow) and SiO_4 -tetrahedra (blue) are shown in Fig. 3. The free corners of the SiO_4 -tetrahedra point out of the sheet formed by the chains (Burns 2005; Plášil 2018a). This arrangement eventually allows for two possible orientations of tetrahedron corner points as marked in Fig. 3a, b: either *out of* the plane – denoted up (*u*), or *into* the plane – denoted down (*d*), following the description given in Plášil (2018a). Note, from the point of view of topology, both orientations are equivalent (Burns 2005; Plášil 2018a). However, distributions of up and down oriented tetrahedra is apparently only favored energetically to result in *two* polymorphs of uranophane: while in uranophane- α succession of SiO_4 -tetrahedra along a (UO_7) -chain follows the simple motif *..ud..*, the motif is doubled in the case of uranophane- β , giving *..uudd..* (Fig. 3a, b).

Based on these characteristic motives, structural complexity of uranophane- β was shown to be twice that of uranophane- α (Plášil 2018b; Colmenero et al. 2019). Note that the two characteristic motives lead to an important difference in symmetry. Focusing on one particular (UO_7) -unit in uranophane- α , orientations of the SiO_4 -tetrahedra of the two directly adjacent (UO_7) -units along the chain are identical (both up or both down), opposing the orientation of the SiO_4 -tetrahedron at the particular (UO_7) -unit in focus (compare Fig. 3a). In the case of uranophane- β , the orientation of those two neighboring SiO_4 -tetrahedra is diametrical opposed (one up, the other down; Fig. 3b). Therefore, we expect differences in the spectra of the two uranophane polymorphs.

Sklodowskite structure belongs to spacegroup $C2/m$ and follows as well the sheet structure of uranophane topology. It shares its main characteristic with uranophane- α , especially the building motif *..ud..* (Fig. 3c; Mokeeva 1964; Ryan and Rosenzweig 1977; Burns 2005; Plášil 2018a). Notably, no second polymorph of sklodowskite exists.

Haiweeite – spacegroup $Pbcn$ – on the other hand does not belong to the uranophane topology, even though it shares the existence of (UO_7) -chains linked to SiO_4 -tetrahedra (McBurney and Murdoch 1959; Burns, 2001; Plášil et al., 2013). Yet, in haiweeite these structural elements form a more complex network, where the orientations of the SiO_4 -tetrahedra sharing edges with (UO_7) -bipyramids remain conserved along the chain (Fig. 3d).

2.2 Raman-Spectroscopy

Measured Raman spectra of the minerals under investigation are shown in Fig. 4 together with reference-data taken from the ruff-project (ruff.info; Lafuente et al. 2015). We focus on spectral range from approximately 750 cm^{-1} to 1100 cm^{-1} . Here, the most prominent and discriminating spectral features

become visible. As Raman-bands are associated with vibrational modes, closer analysis of the spectra yields valuable data discussing phononic contributions to luminescence spectra.

The dominant peak around 790 cm^{-1} is associated to stretching vibrations ν_1 of the (linear) UO_2^{2+} , while bands in the range of 930 cm^{-1} to 980 cm^{-1} are associated with stretching vibrations of the SiO_4 -tetrahedra (Frost et al. 2006a; 2006b; 2006c; 2006d; Wall et al., 2010; Colmenero et al., 2018; Colmenero et al., 2019).

As expected from structural similarities, the phonon energies of the UO_2^{2+} vibration in the uranyl-silicates under investigation are close to each other, because peak-shifts are mainly induced by the equatorial ligand field of UO_2^{2+} (Pierloot and van Besien 2005). Especially, the two polymorphs of uranophane show almost identical phonon energies. In the range 930 cm^{-1} to 980 cm^{-1} , Raman spectra of the different species show distinct differences associated to vibrations of the SiO_4 -tetrahedra. In line with their structural equivalence, sklodowskite and uranophane- α exhibit pronounced similarity at this band. In the case of uranophane- β , the band is shifted to lower energies, reflecting its deviating building motif *..uudd..*. Eventually, the significantly different structure of haiweeite results in a distinct Raman signature in that range.

2.3 Luminescence-Spectroscopy

Spectroscopic data on uranophane- α , uranophane- β , sklodowskite and haiweeite have been reported under varying conditions on natural crystals as well as on synthetic material. Despite the broad range of literature in this field, only few data sets are freely accessible. Luminescence spectra were already investigated by Haberlandt and colleagues (1950) with further assignment to mineral species by Meixner (1965). Later data refers to spectra obtained as well on naturally grown (Cunnane et al. 1993; Gorobets 2002; Wang et al. 2005; Frankland et al. 2022) as on synthesized material (Lehmann et al. 2008; Kuta et al. 2013). Table 2 provides a compilation of available data together with our own values. We are aware that this listing is not complete, yet tendencies can be seen.

Table 2
Emission lines of the minerals in this study

Mineral	Peak positions [nm]	Remark	Ref.
Uranophane- α	515, 536, 557	77K ^b	Gorobets 2002
	511, 532, 552	77K ^b	Gorobets 2002
	484.5, 493.8, 512.3, 533.2, 555.6, 580.1	synth. crystals	Lehmann et al. 2008
	(493 + 501), (513 + 524), 535, 560, 590, 624	assigned by Meixner, 1965	Haberlandt et al. 1950
	(493 + 501), (513 + 520), (535 + 539), 558	from figure; synth. double peaks	Kuta et al, 2013 Frankland et al. 2022
	477.4, (492.2 + 499.0), (512.1 + 518.9), (533.4 + 540.7), (555.7 + 564.8) 493, 513, 535, 557, (588)	base spectrum^a	this work
Uranophane- β	501, 521, 544, 569, 600, 630	assigned by Meixner, 1965	Haberlandt et al. 1950
	503.1, 525.5, 547.0, 570.5	5.5 K ^b	Wang et al. 2005
	500, 520, 542, 566, 592	base spectrum^a	this work
Sklodowskite	520, 535, 550	77K ^b	Gorobets 2002
	505, 525, 548, 571	taken from figure	Cunnane et al., 1993
	496.6, 516.7, 538.7, 561.5	5.5 K ^b	Wang et al. 2005
	(490), 505, 525, 547, 571, 598	base spectrum^a	this work
Haiweeite	506, 528, 552, 577, 608, 640	assigned by Meixner, 1965	Haberlandt et al. 1950
	505, 526, 547	base spectrum^a	this work

^a Details see text. ^b Different conditions of measurement.

Remarkably, three reports give evidence of a double-peak structure for uranophane- α , notably for natural crystals (Haberlandt et al., 1950; Frankland et al. 2022) as well as for synthetic material (Kuta et al., 2013). Data presented by Wang et al. (2005) is rather assigned to uranophane- β : while only 'uranophane' is specified in the text, uranophane- β is mentioned there in the legend of the second figure. Further observations by Frankland and colleagues (2022) support such assignment.

The emission spectrum of UO_2^{2+} in a well-ordered crystal with only little defects consists of a clear band structure with a succession of (rather sharp) phononic peaks (Cunnane et al. 1993; Lehmann et al. 2008; Drobot 2015a; Višňák and Sobek 2016; Haubitz et al. 2018). In the following, we outline the model described separately by Drobot (2015a) as well as by Višňák and Sobek (2016). Figure 5 shows a simplified representation of the relevant electronic ground- and excited state together with phononic levels (Višňák and Sobek 2016). Optical relaxations occur from the bottom of the excited state to one of the phononic levels of the ground state, where the phonon energy ω_{phonon} is equivalent to the $(\text{UO}_2)^{2+}$ stretching vibration as determined by Raman spectroscopy (Drobot, 2015a; Višňák and Sobek 2016; Colmenero et al., 2018). The transition without contribution of a phonon, i.e. from the bottom of the excited state to the bottom of ground state (denoted $0' \rightarrow 0$, following Višňák and Sobek 2016), defines the zero-phonon line (ZPL), which is the characteristic transition of this system (Drobot 2015a; Višňák and Sobek 2016; Haubitz et al. 2018). Thus, starting from the zero-phonon line, the further peaks of the spectrum are determined by multiples of the phonon energy. Note, the more phonons are necessary to balance the transition energy, the less likely this transition will be, so emitted intensity will decrease with phonon number (Višňák and Sobek 2016). Considering the phononic levels of the excited electronic state, (i) their energy separation ω'_{phonon} is equidistant, but will differ from ω_{phonon} of the ground state (due to the fact that the excited state is more extended) and (ii) the occupation follows a Boltzmann distribution (Višňák and Sobek 2016). Thus, there is a small possibility, that “hot-band” transitions occur, starting from the first phononic level of the excited electronic state ($1'$) to one of the phononic-levels of the fundamental electronic state (see Fig. 5; Drobot, 2015a; Višňák and Sobek 2016). According to Boltzmann–distribution, we can assume transitions from the first phononic level only, which in good approximation will not carry more than a few % of the intensity (Višňák and Sobek 2016; Haubitz et al. 2018). For the same reason as for the main phononic peak series, we have to assume hot-band contributions to decrease well with number of phonons involved. Thus, the transition from the first phononic level of the excited electronic state to the bottom of the fundamental electronic state, $1' \rightarrow 0$, is the dominant hot-band. It occurs at higher energy as compared to the zero-phonon line ($0' \rightarrow 0$), but with much lower intensity (Višňák and Sobek 2016; Haubitz et al. 2018). In first approximation, a spectrum composed according to these considerations consists of the sequence of main phononic bands with intensities decreasing with decreasing energies and separated by ω_{phonon} , plus a down-scaled copy of this sequence, shifted by ω'_{phonon} , representing hot-band contributions (Drobot 2015a; Višňák and Sobek 2016; Haubitz et al. 2018).

We follow Drobot (2015a) to illustrate the model with a synthetic spectrum as depicted in Fig. 6. We assume Lorentzian peak-shapes, the zero-phonon line at 500 nm (2.48 eV), phononic energy ω_{phonon} of 99 meV as given by $(\text{UO}_2)^{2+}$ stretching vibrations and determined by Raman-spectroscopy (see Colmenero et al. 2019), an empiric width of the phononic peaks of 25 meV (compare Drobot et al. 2015b) and an empiric hot-phonon energy ω'_{phonon} of 60 meV with hot-band intensity of about 5% of the total intensity. Intensity of the phononic bands follows mainly the sequence 1:1:0.5:0.25:0.1 (compare Višňák

and Sobek 2016). The resulting artificial spectrum already covers main characteristics of generic uranyl emission.

Even though the outlined model was developed for uranyl-ions in solution interacting with ligands, it represents a surprisingly good approximation in the case of uranyl-silicates. Here, we introduced the model in first place to explain spectral features and to lay the fundamentals for further discussion rather than to provide fitted data.

3 Materials And Methods

3.1 Samples

Samples from different localities are of the authors' collections, or were kindly provided by various private collectors. Table 3 lists locations and samples. All samples have been examined visually to exclude obvious misidentifications and to check for luminescing contaminations. For a series of samples, energy dispersive x-ray spectroscopy (EDS), Raman analysis and x-ray diffraction (XRD) have been performed to ensure assignment of the minerals. As outlined above, especially Raman analysis was found a useful technique for fast assignments of larger number of samples (Frost et al. 2006a-d; Wall et al. 2010; Colmenero et al. 2018; Colmenero et al. 2019).

Table 3
List of samples investigated together with the locations

Mineral	Location	Quantity
Uranophane- α		48
	Kaiserer quarry, Rauris valley, Austria	1
	Madawaska Mine, Ontario, Canada	2
	Shinkolobwe, Haut-Katanga, DR Congo	1
	Musonoi mine, Lualaba, DR Congo	4
	Les Bois-Noirs, Loire, France	3
	Menzenschwand, Baden-Württemberg, Germany	13
	Clara mine, Oberwolfach, Baden-Württemberg, Germany	5
	Wölsendorf, Bavaria, Germany	6
	Hagendorf, Bavaria, Germany	1
	Großschloppen, Bavaria, Germany	2
	Mechelgrün, Saxony, Germany	1
	Arcu su Linnarbu, Sardinia, Italy	3
	Limes, Trentino-Alto Adige, Italy	1
	Montoso Quarries, Piedmont, Italy	1
	Bong Mine, Bong Town, Liberia	1
	Eureka Mine, Lleida, Catalonia, Spain	3
Uranophane- β		12
	Pasel adit, Radhausberg, Bad Gastein, Austria	4
	Perus, São Paulo, Brazil	3
	Barbora adit, Jáchymov, Czech Republic	1
	Wölsendorf, Bavaria, Germany	1
	Montoso Quarries, Piedmont, Italy	1
	Nopal, Chihuahua, Mexico	1
	Rössing uranium mine, Erongo Region, Namibia	1
Sklodowskite		17
	Shinkolobwe, Haut-Katanga, DR Congo	1

Mineral	Location	Quantity
	Clara mine, Oberwolfach, Baden-Württemberg, Germany	12
	Paliokamariza mines, Lavrion Mining District, Greece	3
	Descuido mine, Barranco Hondo, Andalusia, Spain	1
Haiweeite		9
	Pasel adit, Radhausberg, Bad Gastein, Austria	2
	Perus, São Paulo, Brazil	2
	Teófilo Otoni, Minas Gerais, Brazil	2
	Los Azules mine, Atacama, Chile	1
	Dara-i-Pioz Glacier, Tajikistan	1
	Coso Mts., Haiwee Reservoir, California, USA	1

3.2 Sample characterization

Sample characterization (service purchased from Mineralanalytik Eu, Germany) was performed by Raman, EDX and/or XRD measurements. The Raman system (Horiba XploRa Raman microscope) was mainly used with 532 nm excitation. To reduce influence of luminescence, 785 nm excitation was used where necessary. Typical spotsizes on the sample were about 2 μm and smaller, ensuring measurement on individual crystallites. For elemental analysis, REM-EDX was used (Hitachi S3700N together with Bruker Quantax200). Samples were measured at 20 kV acceleration voltage and at a residual pressure of 40 Pa to reduce skirt effect and surface charging. Structural determination was done by powder x-ray diffraction (Rigaku Miniflex benchtop system) in Bragg-geometry with Cu K_{α} -source.

Additionally, confocal Raman microscopy at 532 nm excitation wavelength has been applied on selected samples (alpha300 R; WITec GmbH, Ulm, Germany; equipped with a Nd:YAG laser operated at 3 mW; objective x20 NA0.75; system established at the Institute of Materials Science, Physics of Surfaces, Technical University of Darmstadt, Germany).

3.3 Epiluminescence spectrometer with light sheet excitation application

Spectral data have been acquired using an epiluminescence spectrometer setup at ambient conditions with optional light sheet excitation, adapted to the investigation of uranyl-luminescence in solid state samples. It is designed as slit spectrometer (25 μm entrance slit) with a 15x NA0.28 Beck/Ealing reflecting objective for UV applications. A longpass filter (Chroma LP435) blocks the excitation light. The light is collimated (75mm f/4 achromatic collimator) onto a combined dispersive element (grism, a combination of transmission grating with 600 lines/mm and prism; dismantled material, unknown manufacturer), which results in a rather compact set-up. The spectrum is imaged by a cooled

monochrome CCD camera (1392x1040 pixel, sensor Sony ICX285AL, camera Starlight Xpress Trius) using a 60mm f/4 apochromatic objective (Apo-Componon, Schneider Kreuznach).

For excitation of crystal aggregates, a condensed LED (Nichia NVSU233A-D1 with nominal peak wavelength of 365 nm and half width at full maximum of around 8 nm) together with a dichroic beam splitter (Chroma AT440DC) were used. The excitation wavelength was additionally filtered (Schott UG1) to suppress contributions in the visible.

Spatially resolved measurements on individual crystals were achieved by a light sheet excitation scheme. Here, the light source is a continuous wave diode laser with 405 nm central wavelength and nominally 300 mW optical power (Osram LD). The laser is coupled into a 405 nm single mode fiber by passing a field stop and focused by a microscope objective (20x NA0.5 Olympus HC PL Fluotar). At the fiber output, the beam is first collimated, then expanded and eventually refocused onto the sample (objective: 10x NA0.3; Olympus HC PL Fluotar). A rotatable polarizer provides intensity control. In order to suppress any possible long wavelength contribution, the excitation is filtered by a bandpass clean-up filter (405 nm, Chroma ZET405/20x). Excitation spot sizes have been determined to be in the range of 3 μm to 5 μm in diameter, depending on the scattering behavior of the sample under investigation, with an estimated extension in depth of about 10 μm . Positioning is fully adjustable in order to line-scan an individual crystal. Positioning and focusing were controlled via a second camera.

Wavelength and efficiency calibration of the spectrometer was performed using the solar spectrum and its absorption lines as reproduceable standard. Additionally, a dark correction is applied to each raw luminescence spectrum to eliminate thermal effects from the CCD sensor as well as systematic scattering and autofluorescence.

3.4 Measurement and data analysis

By careful inspection, specimens were chosen such as to exclude possible influence introduced by intergrown material of different species. Crystals on matrix, detached crystal fragments and individual crystals extracted from aggregates have been investigated. No significant influence of the sample type on the measured data was detected.

Aggregates on matrix were directly measured, crystal fragments or individual crystals were prepared onto non-fluorescing double-sided tape for spectroscopic measurements. In all cases, background luminescence was excluded by adapting illumination as well as field and direction of view. In addition to different sizes and qualities of crystal fragments, material from different localities showed strongly varying intensities. Exposure times and illumination intensities were adapted to ensure stable measurement conditions especially concerning noise level and sample integrity. Under the given conditions, no common base could be established to quantify intensity. Therefore, only normalized data are presented and discussed.

Spectra were corrected for possible offset and normalized to the maximum of the ZPL. That type of normalization reflects the concept, that the electronic transition into the electronic ground-state without

contribution of a phonon is the most characteristic and the most conserved. Structural disorder is expected to result in a small red-shift of this transition. Note, this normalization conserves spectral shape and peak positions, but not intensities. In case of the variable double peak structure, commonly observed in uranophane- α , the higher peak was chosen.

Further characterizing parameters are based on an empirical approach. As measure, the centroid wavelength $\lambda_{centroid}$ is introduced, defined according to Eq. (1):

$$\lambda_{centroid}(\lambda_{min} \cdot \lambda_{max}) = \frac{\sum_n I_n \lambda_n}{\sum_n I_n}$$

1
,

where I_n denotes the normalized intensity at data-point number n with respective wavelength λ_n in the range λ_{min} to λ_{max} . As overall measure the global centroid wavelength

$\lambda_{global} = \lambda_{centroid}(485...615nm)$ provides a basic measure for perceived color and respective color shift. The chosen wavelength range is limited to 615 nm to avoid bias by possible contribution of Eu^{3+} luminescence.

Local ordering parameters are defined similarly, measuring the contribution of a possible double peak structure. In the case of uranophane (i.e. uranophane- α and uranophane- β), this quantity is given as

$\lambda_{Uranophane} = \lambda_{centroid}(493...500.5nm)$. Further local ordering parameters

$\lambda_{sklodowskite} = \lambda_{centroid}(503...510nm)$ in the case of sklodowskite and

$\lambda_{haiweeite} = \lambda_{centroid}(505.5...512nm)$ for haiweeite. To remain in the scope of this study, further possible parametrizations are not included.

4 Results

4.1 Spectra of uranophane- α , uranophane- β , sklodowskite and haiweeite

Figure 7 presents spectra of the four mineral species, acquired on individual crystals and aggregates. Clearly, all of the spectra resemble the generic spectrum shown in Fig. 6, in line with the luminescence mechanism outlined. Spectra are normalized to the ZPL, accounting for the characteristic nature of the ZPL. However, intensities are not easily comparable. As general observation we state, that the spectra of the different samples and locations of each species are similar, but to different degrees. While striking variability is obvious in the spectra of uranophane- α (Fig. 7a), the spectra of its polymorph uranophane- β (Fig. 7b) are much more uniform. Similarly, spectra of sklodowskite (Fig. 7c) and haiweeite (Fig. 7d) appear rather stable. A striking feature in the spectra of uranophane- α only is the appearance of a distinct double peak structure (DPS). This is not present in any of the other ensembles, especially not in the case

of sklodowskite. Additionally, broadened features or even loss of structure can be observed for all species accompanied by a global red-shift.

4.2 Individual crystals

Such variations and the appearance of a double-peak structure in the case of uranophane- α is not an effect related to the ensemble measured, but an effect already encountered on the level of individual crystals. To address this, individual crystals extracted from aggregates were investigated scanning along the long crystal axis. With spot-size below 5 μm diameter and estimated elongation in depth of 10 μm for the exciting 405 nm laser beam, 25 μm spacing was chosen to take spectra. Again, for comparison, crystals of uranophane- α , uranophane- β and sklodowskite have been investigated. For all three samples identities have been confirmed by EDS and XRD or Raman spectroscopy. Note, that due to generally small crystal dimensions of available uranophane- β , the scan spans only 100 μm while almost 1000 μm was reached on uranophane- α . As a guide to the eye, spectra at equidistant positions are highlighted in red, see respective figure caption. The spectra of all three species show variations at different positions. However, only in the case of uranophane- α (Fig. 8, sample #086, Menzenschwand, Germany), the evolution of a pronounced double-peak structure is visible with rather localized changes in spectra, e.g. at positions around 100 μm to 150 μm and 625 μm to 675 μm .

For detailed inspection, three spectra are collected in Fig. 9: at 100 μm (#086 – 4), 625 μm (#086 – 26) and 650 μm (#086 – 27). While spectrum 086 – 4 shows only little contribution of a double peak structure, it appears rather prominent in the other two cases. The obvious appearance of a double peak structure (DPS) in the case of trace #086 – 26, even with dominant peak at around 505 nm, is accompanied by a prominent red shift of the peak-positions not only of the ZPL. On the other hand, the leading hot-band transition $1' \rightarrow 0$ hardly changes, neither in position nor in signal contribution. In trace #086 – 27, immediately taken after #086 – 26, the double peak structure is again less prominent and the ZPL matches the one of trace #086 – 4. Note, as data was taken on an individual crystal, those variations are intrinsic to the crystal and not imposed by external influences.

In the cases of uranophane- β (Fig. 10; sample #088, Nopal mine, Mexico) and sklodowskite (Fig. 11; #090, Clara mine, Germany), no indication of a possible double peak structure is visible in the spectra taken on individual crystals. This is in-line with the observation on the data ensembles (Figs. 7b,c)

4.3 Characteristic base spectra

To further analyze these observations, we define the centroid wavelength λ_{global} evaluated in the range of 485–615 nm (details see section 3.3) as global ordering parameter. This quantity is intended to measure global shifts of the spectral fingerprint reflecting to some extent the perceived luminescence color. Lower λ_{global} correspond to perceived green, while higher values indicate shift to yellow/orange. As second quantity, the centroid wavelength $\lambda_{Uranophane}$ evaluated in the range 493...500.5 nm focuses on the absence or presence of a double-peak structure in uranophane. When only little indication of a

double-peak structure is present, $\lambda_{Uranophane}$ will be smaller as compared to the case of a significant contribution. Similarly, local ordering parameters are defined for the other species, as introduced in section 3.3.

Before we discuss the variability mentioned above, we aim at providing spectra basically free of additional contributions, e.g. induced by defects. Those spectra are referred to as *base spectra*. In a crystal with low disorder only a limited number of non-radiative relaxation pathways will contribute. Therefore, average emitted photon-energy will be comparatively high. Hot-bands will be governed by the intrinsic Boltzmann distribution basically lacking alternate mechanisms to promote their contributions.

Thus, base spectra are those with minimal local ordering parameter ($\lambda_{Uranophane}$ in the case of uranophane- α and uranophane- β , $\lambda_{Sklodowskite}$ and $\lambda_{Haiweeite}$ correspondingly for the other mineral species). Resulting base spectra are highlighted red in Fig. 7 and are collected for better visibility in Fig. 12. To stabilize results, those spectra have been excluded from determination of the base spectra, where no clear peak structure of the phononic transitions was visible. Related peak positions of the resulting base spectra are the ones noted in Table 2.

4.4 Spectral variability

Global centroid wavelength λ_{global} serves for rough quantification of the apparent color shift. For haiweeite, λ_{global} covers 525–530 nm, for sklodowskite the range is moderately wider (537–547 nm), while for uranophane- α it spans 520–552 nm and for uranophane- β 524–553 nm. Note, the evaluation range of the global centroid wavelength is limited to exclude contributions of Eu^{3+} , thus underestimates the red part of the spectrum.

With the global change of spectra, peak positions are as well affected. We expect the rising influence of further spectral contributions to indicate a rise in competing relaxation pathways, thus additional broadening and red-shifting of the spectroscopic structures.

For uranophane- α , peak position of the zero-phonon line is plotted in Fig. 13a against parameter $\lambda_{Uranophane}$ used as heuristic order parameter. The peak position shifts from 493 nm to about 498 nm. Along with peak-shift, parameter $\lambda_{Uranophane}$ increases, indicating growing influence of the double-peak structure. Beyond $\lambda_{Uranophane} = 496.55\text{nm}$, the ZPL starts to get drowned in the growing additional peak. In such cases, only this additional peak of the double peak structure is identified, thus giving peak position values around 501 nm. Above $\lambda_{Uranophane} = 496.66\text{nm}$, the ZPL can no longer be identified as separated peak, the additional peak of the double-peak structure finally governs the spectral structure leading to peak positions around 501 nm. The ZPL of the uranophane- β base spectrum is 500 nm: uranophane- α spectra at $\lambda_{Uranophane} > 496.66\text{nm}$ apparently mimic spectra of uranophane- β . This is reflected in Fig. 13b, where the ensemble of uranophane- β (red triangles) meets with data points belonging to uranophane- α (black circles). Inspecting the same relation for the other mineral species, i.e. ZPL-position versus respective local ordering parameters (parameter $\lambda_{Uranophane}$, $\lambda_{Sklodowskite}$ and

$\lambda_{\text{Haiweeite}}$) reveals, that a pronounced peak red-shift is a property of uranophane- α only - basically lacking in the other data sets (Fig. 13b).

5 Discussion

5.1 Spectra and their variability

The measured base spectra of uranophane- α , uranophane- β , sklodowskite and haiweeite as shown in Fig. 8 are expected to be already good estimates for true pure spectra. Both uranophane polymorphs can be distinguished from the closely related sklodowskite as well as from haiweeite on the basis of luminescence spectra. While we are aware that those spectra have been derived from natural material, measured peak positions are well in line with literature values (Table 2). All four mineral species showed some variability in their spectra. Especially, the overall red-shift is a common feature that can be interpreted by an additional defect-induced broadening, possibly related to radiation damage or weathering. Interestingly, the most prominent variability occurs in the case of uranophane- α , especially exhibiting a double peak structure. Our finding of a double peak structure is supported by previous data as well on natural (Haberlandt et al., 1950; Frankland et al. 2022) as on synthetic material (Kuta et al. 2013).

At this point we emphasize, that the prominent double peak structure was observed in the case of uranophane- α *only*, but for *all* uranophane- α available to this study, independent of locations. In several cases, the peak of the second spectral species at around 501 nm dominated the spectrum, reducing the ZPL of uranophane- α (at around 495 nm) to barely more than a “shoulder”. While the luminescence spectrum in such cases might mimic uranophane- β , Raman and XRD-data clearly indicated uranophane- α as main species. For practical use of luminescence spectroscopy e.g. in field-monitoring applications, this observation has to be considered to avoid misinterpreting spectra of uranophane- α as uranophane- β . It might be helpful to explicitly address the absence of this “shoulder” for assignment of uranophane- β (provided accordance in the main spectrum).

5.2 Spectral Reconstruction

To further address the double peak structure observed on uranophane- α , we apply the model outlined in section 2.3. Selected spectra of uranophane- α and uranophane- β are decomposed into respective phononic bands with additional hot-band contributions (Fig. 14). Applying the model, we are aware that in inorganic crystals localized defects and substitutions might introduce changes to the model. An additional contribution to account for general spectral broadening and redshift, thus reflecting general loss of crystallinity or further alteration, might be necessary (Frankland et al. 2022). However, this analysis is not meant as modelling in strict sense, but rather intended to illustrate spectral relations.

As we focus on systematic influences, we chose the base spectra of uranophane- β (spectrum #117-6) and uranophane- α (#086 - 4) together with spectrum #065, a representative uranophane- α spectrum with distinct double-peak structure, but low overall redshift.

First, the spectrum of uranophane- β was parameterized in sequences of phononic and hot-peaks using Lorentzian peak shapes. Positions of the phononic peaks were taken from measured data, their average energetic separation ω_{phonon} of about 97 meV corresponds rather well to the energy of the UO_2^{2+} symmetric stretching vibration as determined by Raman (compared to 99 meV from Colmenero et al., 2019). The sequence of intensities with ratios 0.89:0.93:0.48:0.15:0.03 (compare to Višňák and Sobek 2016) with empiric peak-width of 25 meV delivers already the main characteristics of the spectrum (blue components in Fig. 14a). To estimate hot-peak contributions (compare Fig. 5), the obtained phononic sequence is scaled by 0.06 with empiric width of 30 meV and shifted by the estimated hot phonon energy ω'_{phonon} of 66 meV (magenta components in Fig. 14a). By this scaling we assure, that the hot-band contribution remains limited to several percent. The hot phonon energy estimate is taken from data with the width taken as fitting parameter. The full composed spectrum (red) matches the measured data (black in Fig. 14a) very well.

In a similar manner the base-spectrum of uranophane- α is parameterized (Fig. 13b). Main phononic bands (blue) are characterized by a separation of 98 meV in accordance with Raman data and intensity ratios (0.74:0.76:0.33:0.1:0.02) are similar to those of uranophane- β . Hot band contributions are shifted by 66 meV.

As the contribution of the hot bands to intensity is limited by the Boltzmann distribution to a few percent (Višňák and Sobek 2016; Haubitz et al. 2018), an additional component is necessary. This becomes evident regarding the relative intensities of bands necessary to reconstruct the uranophane- α spectrum. The leading hot-band transition of highest probability ($1' \rightarrow 0$, at around 2.56 eV; Fig. 14b) is comparably small as in the case of uranophane- β . In contrast, the following bands necessary for reconstruction (e. g. $1' \rightarrow 1$, at around 2.48 eV; Fig. 14b) carry a rather large contribution (about half the amplitude of the related phononic band). Assigning those large contributions to multi-phonon hot-bands would contradict thermal limitations – especially as the leading hot-band is of small intensity. Therefore, we conclude that an additional component – a second spectroscopic species – is necessary that shows a phononic structure with a well-defined relation to the phononic bands of uranophane- α .

As empirical observation we state that the spectral fingerprint (peak positions, spacing and relative peak intensities) of this second spectroscopic species (necessary to reconstruct uranophane- α spectra) matches well with the base spectrum of uranophane- β . Thus, we propose to directly use the scaled uranophane- β phononic sequence as additional component representing the second spectroscopic species.

In detail, we reconstruct the uranophane- α spectrum using the main phononic sequence of uranophane- α plus corresponding hot bands (position and spacing from measured data, intensity scaled by 0.06 with respect to phononic peaks) and adding the scaled phononic spectrum of uranophane- β . Here, we use exactly the reconstructed base spectrum of uranophane- β described above (i.e. in the case of #117-6), uniformly scaled by a factor 0.45 (dashed brown bands in Fig. 14b). Again, the composed spectrum (red) matches rather well the measured data (black in Fig. 14b).

In an analogous manner, the spectrum of uranophane- α #065 with prominent double peak spectrum is reconstructed (Fig. 14c). Notably, the ZPL is red-shifted by about 5 meV, separations of the phononic bands (blue in Fig. 14c) are around 95 meV, intensity ratios are 0.38:0.88:0.4:0.12:0.03. Red shift and reduced phononic energy might reflect pronounced presence of defects. Again, following the concept outlined, a small intrinsic hot-band contribution is added (magenta) plus the uniformly scaled (factor 0.72) and shifted (6.5 meV) uranophane- β phononic sequence representing the second spectroscopic species (brown in Fig. 14c). Uniform scaling and the necessity of a uniform shift of the spectrum of the second spectroscopic species shows that the second spectroscopic species is incorporated in the crystal lattice. The reconstructed spectrum (red) approaches the measured data (black in Fig. 14c) rather well, even though some discrepancies become visible. Remarkably, the main phononic contributions are not dominating the double peak structure. Instead, the spectrum seems more related to uranophane- β .

5.3 Incorporated clusters of uranophane- β as proposed origin

The pronounced spectral variability of uranophane- α with respect to the other two uranyl silicates haiweeite and sklodowskite points to a pronounced variability on structural level, as the uranyl luminescence is sensitive to its local environment. We briefly summarize the observations concerning the second spectroscopic species.

Reconstructing spectra of uranophane- α , a second spectroscopic species is necessary to limit hot-band contributions within thermal constraints. This second spectroscopic species is well described by the uniformly scaled phononic sequence of uranophane- β and it red-shifts with the shift of the uranophane- α phononic peaks. Additionally, this signature occurs and varies locally on individual crystals. Thus, the species is incorporated in the uranophane- α crystal. The contribution of a second spectroscopic species was observed to variable degree in all uranophane- α spectra taken from samples of 16 different locations and the spectral characteristics of the second spectroscopic species is conserved in the related data (see Fig. 7). Thus, we exclude chemical substitutions as direct source of the spectral contribution, as the double peak structure appears with one systematic signature, only varying in intensity. Next, the spectrum of the second spectroscopic species is well represented by (the phononic sequence of) the base spectrum of uranophane- β . The pronounced and variable double peak structure occurred in the case of uranophane- α only. We emphasize that none of the examined uranophane- α samples showed a spectrum, where a contribution of uranophane- β could be excluded. No such double peak structure was visible in the spectra of sklodowskite or haiweeite – for both species no polymorphic forms exist either.

In this light, the hypothesis of strongly varying hot-band contributions as explanation seems unsatisfactory. Such variations should similarly occur in the other mineral species, especially of equivalent uranophane topology, i.e. in sklodowskite. However, this is not observed.

Likely, a possible contribution of a second type of UO_2^{2+} luminescent center should apply as well in the case of uranophane- β and sklodowskite, thus not explaining the exclusive behavior of uranophane- α .

Therefore, we propose, that indeed small clusters of a uranophane- β like phase are present in uranophane- α to varying degree. As both uranophane share chemistry and topology, such defects – essentially exchanging locally the building sequence *..udud..* by *..uudd..* – might be stabilized by the polymorphism. Those clusters contribute to the luminescence with their respective spectra. The photon energy corresponds to the photon energy of uranophane- α hot-band luminescence, allowing for energy transfer. As these clusters represent defect structures incorporated in the uranophane- α lattice, the spectral signature shifts with the overall spectral red-shift in a disturbed lattice.

Regarding the reverse case of uranophane- α clusters in uranophane- β , no contribution to the spectrum is expected. The bandgap energy of uranophane- α is larger than that of uranophane- β (2.68 eV, Colmenero et al. 2019), related to a higher ZPL energy of uranophane- α as compared to uranophane- β . Additionally, spectral features of uranophane- α do not match hot-bands of uranophane- β hampering reverse energy transfer.

For sklodowskite, no such mechanism is observable, as no polymorphic form exists. Haiweeite on the other hand has a different topology, so the reasoning is not simply transferable.

Our hypothesis of uranophane- β like clusters incorporated in uranophane- α is supported by observations by Wall and colleagues (2010), who report traces of uranophane- β in synthesis of uranophane- α .

5.4 Polymorphism and spectral variability: possible relations

Looking at UO_2^{2-} in the well-defined environment of sklodowskite, all possible sites are predetermined (neglecting obvious defects like vacancies or impurities). The situation in uranophane is slightly different, as two polymorphs exist. Without obvious defects like vacancies or impurities, a localized transition between the two characteristic structures uranophane- α and uranophane- β might be possible. The uranophane topology is conserved in both cases. We consider the characteristic structural elements of the two uranophane structures: an alternating succession of up- and down-oriented SiO_4 -tetrahedra (Fig. 2). While the characteristic motif of uranophane- α is *..ud..* the equivalent motif of uranophane- β is *..uudd..* Thus, at the growth front or at a domain interface, seeds of uranophane- β structure might readily form simply by misorientation or stacking defects of one chain unit, so e.g. *..ududu* becomes by addition of one unit *..ududuu*, where the occurrence of *uu* might already favor continuation in uranophane- β type phase.

Colmenero and colleagues (2019) showed uranophane- α to be the thermodynamically slightly preferred form of uranophane. So, a seed of uranophane- β structure in uranophane- α is not favored and growth will be limited by thermodynamic conditions. Small variations rapidly stop further propagation of this domain. On the other hand, the energy difference appears to be rather low, -12.0 kJmol^{-1} at zero temperature and pressure according to Colmenero and colleagues (2019). Thus, further variations in environmental conditions might again support reappearance of a uranophane- β domain, its growth eventually again being stopped and so forth. Such a mechanism might produce small, randomly

distributed but localized domains of uranophane- β like phases in the general uranophane- α structure. Notably, the mechanism might occur similarly under natural as well as under laboratory conditions of crystal growth. The scenario described here is supported by the observation of typically different morphology of natural uranophane- α (crystals with high aspect ratio) with respect to that of natural uranophane- β (more bulky crystals), indicating differences in growth mechanisms and pointing to a rather fast growth of uranophane- α crystals (Schindler et al. 2004; Schindler et al. 2004b). Additionally, approaches to obtain uranophane- β by synthesis resulted rather in uranophane- α phase (Cesbron et al., 1993).

As potential second pathway, intrinsically induced radiation damage and healing of related defects might play their role (Utsunomiya et al. 2003; Sureda et al. 2011). By radioactive decay, structure is damaged while the chemical elements basically remain at the site, thus particle numbers can be regarded as approximately conserved. Under the condition, where no particles can be imported, healing of such defects might differ from growth in an open system. Even though this is rather speculative, some support comes from comparison to other systems (Nasdala et al., 2013; Lenz and Nasdala 2015; Lenz et al., 2020).

The situation is substantially different in the cases of sklodowskite and haiweeite. No polymorphic forms are available during growth or restructuring. Thus, a defect site created by a disturbance remains restricted to a point defect, as growth is not supported by a second polymorphic structure, or it vanishes. In consequence, structural variations that affect luminescence emission remain very limited. Thus, spectra are conserved to a higher degree in the case of sklodowskite and haiweeite as compared to uranophane- α .

6 Conclusion

In this study, the uranyl-silicates uranophane- α , uranophane- β , sklodowskite and haiweeite from more than 30 different localities in total have been investigated by optical spectroscopy. By determining spectra with maximum ZPL energy, we identified base spectra of each species representing a relevant approximation of the spectra of the pure mineral phases.

In their pure form, the spectra of the four minerals are clearly measurable and well distinct. For uranophane- β , sklodowskite and haiweeite, only low variability is observed in comparison to spectra of uranophane- α . Spectra of uranophane- α show – to varying degree – a prominent double peak structure. We propose to attribute those contributions to uranophane- β like domains incorporated into uranophane- α , induced by ordering defects and supported in growth by the polymorphism of uranophane. Such a double peak structure was neither observed in the structural related sklodowskite, where no polymorph exists, nor in the chemically related but structurally different haiweeite.

Our approach to relate structure with spectroscopic properties in the case of uranophane might well be transferable to other systems and give insight in growth and decay processes of luminescing uranyl

minerals. To progress further, microanalytical methods like confocal microscopy and transmission electron microscopy are highly desired to verify the existence of uranophane- β domains in uranophane- α .

Finally, we like to emphasize that this study was entirely conducted in the spirit of a citizen science project by the authors and is neither linked to, nor funded by, any academic institution or project in industry. We warmly welcome any effort to further continue this work.

Declarations

Statements and Declarations

The authors have no competing interests to declare that are relevant to the content of this article. The study was entirely funded by private resources of the authors.

Acknowledgements

We thank Jakub Plášil (Department of Structure Analysis, Institute of Physics, ASCR, Czech Republic) for encouraging discussions on the topic and critically reading the manuscript, Robin Steudtner for interesting input concerning modelling and Joy Désor (Mineralanalytik Eu) for his fast and reliable support with EDS, XRD and Raman analysis. We kindly acknowledge access to confocal Raman microscopy provided by Robert W. Stark and Alexander Erb (Institute of Materials Science, Physics of Surfaces, Technical University of Darmstadt, Germany).

We are grateful to all who contributed additional samples, thus making this study possible (in alphabetic order):

†H.W. Bültemann, J. Désor, †G. Eigler, J. Härer, A. Matthies, R. Motzigemba, J. Penzkofer, F. Schimak, S. Stolze and F. Wagner.

References

1. Arnold, T., Baumann, N., Krawczyk-Bärsch, E., Brockmann, S., Zimmermann, U., Jenk, U., Weiß, S. (2011). Identification of the uranium speciation in an underground acid mine drainage environment. *Geochimica et Cosmochimica Acta*, 75(8), 2200-2212.
2. Barinova, A. V., Rastsvetaeva, R. K., Sidorenko, G. A., Pushcharovskii, D. Y. (2001). Crystal structure of high-symmetry α -uranophane. *Doklady Chemistry* 378, 122-124.
3. Barinova, A. V., Rastsvetaeva, R. K., Sidorenko, G. A., Verin, I. A. (2003). Crystal structure of β -uranophane from the Transbaikal region and its relation to the structure of the α modification. *Crystallography Reports*, 48(1), 12-15.
4. Blasse, G. (1987). On the emission colour of the luminescence of hexavalent uranium in oxides. *Inorganica chimica acta*, 129(1), 115-118.

5. Burns, P. C., Miller, M. L., Ewing, R. C. (1996). U^{6+} minerals and inorganic phases; a comparison and hierarchy of crystal structures. *The Canadian Mineralogist*, 34(4), 845-880.
6. Burns, P. C. (2001). A new uranyl silicate sheet in the structure of haiweeite and comparison to other uranyl silicates. *The Canadian Mineralogist*, 39(4), 1153-1160.
7. Burns, P. C. (2005). U^{6+} minerals and inorganic compounds: insights into an expanded structural hierarchy of crystal structures. *The Canadian Mineralogist*, 43(6), 1839-1894.
8. Cesbron, F., Ildefonse, P., Sichere, M. C. (1993). New mineralogical data on uranophane and β -uranophane; synthesis of uranophane. *Mineralogical Magazine*, 57(387), 301-308.
9. Collins, R. N., Saito, T., Aoyagi, N., Payne, T. E., Kimura, T., Waite, T. D. (2011). Applications of Time-Resolved Laser Fluorescence Spectroscopy to the Environmental Biogeochemistry of Actinides. *Journal of environmental quality*, 40(3), 731-741.
10. Colmenero, F., Timón, V., Bonales, L. J., Cobos, J. (2018). Structural, mechanical and Raman spectroscopic characterization of the layered uranyl silicate mineral, uranophane- α , by density functional theory methods. *Clay Minerals*, 53(3), 377-392
11. Colmenero, F., Plášil, J., Sejkora, J. (2019). The layered uranyl silicate mineral uranophane- β : crystal structure, mechanical properties, Raman spectrum and comparison with the α -polymorph. *Dalton Transactions*, 48(44), 16722-16736.
12. Cunnane, J. C., Gill, V. R., Lee, S. Y., Morris, D. E., Nickelson, M. D., Perry, D. L., Tidwell, V. C. (1993). Uranium soils integrated demonstration: Soil characterization project report (No. FEMP/SUB-058). Fernald Environmental Restoration Management Corp., Cincinnati, OH (United States); Fluor Daniel Environmental Restoration Management Corp., Fernald, OH (United States).
13. DeNeufville, J. P., Kasdan, A., Chimenti, R. J. L. (1981), "Selective detection of uranium by laser-induced fluorescence: a potential remote-sensing technique. 1: Optical characteristics of uranyl geologic targets" *Applied Optics* Vol. 20, Issue 8, pp. 1279-1296.
14. Drobot, B. (2015a), Entwicklung und Validierung mathematischer Methoden zur Auswertung spektroskopischer Daten der Uranyl(VI)-Hydrolyse, Ph.D. thesis, Technical University of Dresden. 146 pp., 2015
15. Drobot, B., Steudtner, R., Raff, J., Geipel, G., Brendler, V., Tsushima, S. (2015b). Combining luminescence spectroscopy, parallel factor analysis and quantum chemistry to reveal metal speciation—a case study of uranyl (VI) hydrolysis. *Chemical science*, 6(2), 964-972.
16. Frankland, V. L., Milodowski, A. E., Bright, J. W., Read, D. (2021). The use of Raman and TRLF spectroscopy for differentiating early stage alteration products of spent nuclear fuel. *Applied Geochemistry*, 130, 104934.
17. Frankland, V. L., Rickman, S. P., Milodowski, A. E., Read, D. (2022). Characterisation of Uranophane and Boltwoodite by Raman, luminescence and laser-induced breakdown spectroscopy. *Applied Geochemistry*, 138, 105183.
18. Frondel, C. (1958). Systematic mineralogy of uranium and thorium (Geol. Survey Bulletin Vol. 1064). US Government Printing Office.

19. Frost, R. L., Čejka, J., Weier, M. L., Martens, W. (2006a). Molecular structure of the uranyl silicates—a Raman spectroscopic study. *Journal of Raman Spectroscopy*, 37(4), 538-551.
20. Frost, R. L., Čejka, J., Weier, M. L., Martens, W. N. (2006b). Raman spectroscopy study of selected uranophanes. *Journal of molecular structure*, 788(1-3), 115-125.
21. Frost R L, Čejka J, Weier M L, Martens W, Klopogge J T (2006c) A Raman and infrared spectroscopic study of the uranyl silicates - weeksite, soddyite and haiweeite. *Spectrochimica Acta Part A- Molecular and Biomolecular Spectroscopy* 64, 308-315
22. Frost, R. L., Čejka, J., Weier, M. L., Martens, W. (2006d). A Raman and infrared spectroscopic study of the uranyl silicates—Weeksite, soddyite and haiweeite: Part 2. *Spectrochimica Acta Part A: Molecular and Biomolecular Spectroscopy*, 63(2), 305-312.
23. Geipel, G., Bernhard, G., Rutsch, M., Brendler, V., Nitsche, H. (2000). Spectroscopic properties of uranium (VI) minerals studied by time-resolved laser-induced fluorescence spectroscopy (TRLFS). *Radiochimica Acta*, 88(9-11), 757-762.
24. Ginderow, D. (1988). Structure de l'uranophane alpha, $\text{Ca}(\text{UO}_2)_2(\text{SiO}_3\text{OH}) \cdot 2.5 \text{H}_2\text{O}$. *Acta Crystallographica Section C: Crystal Structure Communications*, 44(3), 421-424.
25. Gorobets, B. S. (2002). *Luminescent Spectra of Minerals: Reference-book*. RPC VIMS.
26. Görrler-Walrand, C., De Houwer, S., Fluyt, L., Binnemans, K. (2004). Spectroscopic properties of uranyl chloride complexes in non-aqueous solvents. *Physical Chemistry Chemical Physics*, 6(13), 3292-3298. 10.1039/b317002k
27. Haberlandt, H., Hernegger, F., Scheminzky, F. (1950). Die Fluoreszenzspektren von Uranmineralien im filtrierten ultravioletten Licht. *Spectrochimica acta*, 4(1), 21-35.
28. Haubitz, T., Tsushima, S., Steudtner, R., Drobot, B., Geipel, G., Stumpf, T., Kumke, M. U. (2018). Ultrafast Transient Absorption Spectroscopy of UO_2^{2+} and $[\text{UO}_2\text{Cl}]^+$. *The Journal of Physical Chemistry A*, 122(35), 6970-6977.
29. Kuta, J., Wang, Z., Wisuri, K., Wander, M. C., Wall, N. A., Clark, A. E. (2013). The surface structure of α -uranophane and its interaction with Eu (III)—An integrated computational and fluorescence spectroscopy study. *Geochimica et Cosmochimica Acta*, 103, 184-196.
30. Lafuente B, Downs R T, Yang H, Stone N (2015). The power of databases: the RRUFF project. In: *Highlights in Mineralogical Crystallography*, T Armbruster and R M Danisi, eds. Berlin, Germany, W. De Gruyter, pp 1-30; www.rruff.info.
31. Lehmann, S., Geipel, G., Foerstendorf, H., Bernhard, G. (2008). Syntheses and spectroscopic characterization of uranium (VI) silicate minerals. *Journal of Radioanalytical and Nuclear Chemistry*, 275(3), 633-642. <https://doi.org/10.1007/s10967-007-7060-z>.
32. Lenz, C., Nasdala, L. (2015). A photoluminescence study of REE^{3+} emissions in radiation-damaged zircon. *American Mineralogist*, 100(5-6), 1123-1133.
33. Lenz, C., Belousova, E., Lumpkin, G. R. (2020). The In-Situ Quantification of Structural Radiation Damage in Zircon Using Laser-Induced Confocal Photoluminescence Spectroscopy. *Minerals*, 10(1),

83. <https://doi.org/10.3390/min10010083>
34. Massuyeau, F., Perry, D. L., Kalashnyk, N., Faulques, E. (2017). Spectroscopic markers for uranium (VI) phosphates. Part II: the use of time-resolved photoluminescence. *RSC advances*, 7(2), 919-926. <https://doi.org/10.1039/C6RA26157D>
35. McBurney, T. C., Murdoch, J. (1959). Haiweeite, a new uranium mineral from California. *American Mineralogist: Journal of Earth and Planetary Materials*, 44(7-8), 839-843.
36. Meinrath, G. (1997). Uranium (VI) speciation by spectroscopy. *Journal of Radioanalytical and Nuclear Chemistry*, 224(1-2), 119-126.
37. Meinrath, A., Schneider, P., Meinrath, G. (2003). Uranium ores and depleted uranium in the environment, with a reference to uranium in the biosphere from the Erzgebirge/Sachsen, Germany. *Journal of Environmental Radioactivity*, 64(2-3), 175-193.
38. Meixner, H. (1965). Die Uranminerale um Badgastein, Salzburg, im Rahmen Österreichs. – *Sitzungsberichte der Akademie der Wissenschaften mathematisch-naturwissenschaftliche Klasse* – 174: 203 – 227.
39. Mokeeva, I.V. (1964). The structure of sklodowskite, *Soviet Physics - Crystallography*, 9, 217-218.
40. Momma, K., Izumi, F. (2011). VESTA 3 for three-dimensional visualization of crystal, volumetric and morphology data. *Journal of applied crystallography*, 44(6), 1272-1276.
41. Moulin, C., Laszak, I., Moulin, V., Tondre, C. (1998). Time-resolved laser-induced fluorescence as a unique tool for low-level uranium speciation. *Applied Spectroscopy*, 52(4), 528-535.
42. Mühr-Ebert, E. L., Wagner, F., Walther, C. (2019). Speciation of uranium: Compilation of a thermodynamic database and its experimental evaluation using different analytical techniques. *Applied geochemistry*, 100, 213-222.
43. Nasdala, L., Grambole, D., Ruschel, K. (2013). Review of effects of radiation damage on the luminescence emission of minerals and the example of He-irradiated CePO₄. *Mineralogy and Petrology*, 107(3), 441-454.
44. Nelson, J. (2009). Enhanced environmental detection of uranyl compounds based on luminescence characterization, Ph.D. thesis, Virginia Commonwealth University, Richmond, Virginia, 189 pp., 2009.
45. Pierloot, K., van Besien, E. (2005). Electronic structure and spectrum of UO₂²⁺ and UO₂Cl₄²⁻. *The Journal of chemical physics*, 123(20), 204309.
46. Plášil, J., Fejfarová, K., Čejka, J., Dušek, M., Škoda, R., Sejkora, J. (2013). Revision of the crystal structure and chemical formula of haiweeite, Ca (UO₂)₂ (Si₅O₁₂)(OH)₂ · 6H₂O. *American Mineralogist*, 98(4), 718-723.
47. Plášil, J. (2018a). Mineralogy, Crystallography and Structural Complexity of Natural Uranyl Silicates. *Minerals*, 8(12), 551.
48. Plášil, J. (2018b). Structural complexity of uranophane and uranophane-β: implications for their formation and occurrence. *European Journal of Mineralogy*, 30(2), 253-257.

49. Romanchuk, A. Y., Vlasova, I. E., Kalmykov, S. N. (2020). Speciation of uranium and plutonium from nuclear legacy sites to the environment: A mini review. *Frontiers in chemistry*, 630.
50. Ryan, R.R., Rosenzweig, A. (1977). Sklodowskite, $\text{MgO} \cdot 2\text{UO}_3 \cdot 2\text{SiO}_2 \cdot 7\text{H}_2\text{O}$. *Cryst. Struct. Commun.*, 6, 611–615.
51. Schindler, M., Mutter, A., Hawthorne, F. C., Putnis, A. (2004a). Prediction of crystal morphology of complex uranyl-sheet minerals. I. Theory. *The Canadian Mineralogist*, 42(6), 1629-1649.
52. Schindler, M., Mutter, A., Hawthorne, F. C., Putnis, A. (2004b). Prediction of crystal morphology of complex uranyl-sheet minerals. II. Observations. *The Canadian Mineralogist*, 42(6), 1651-1666.
53. Stohl, F. V., Smith, D. K. (1981). The crystal chemistry of the uranyl silicate minerals. *American Mineralogist*, 66(5-6), 610-625.
54. Sureda, R., Casas, I., Giménez, J., de Pablo, J., Quinones, J., Zhang, J., Ewing, R. C. (2011). Effects of Ionizing Radiation and Temperature on Uranyl Silicates: Soddyite $(\text{UO}_2)_2(\text{SiO}_4)(\text{H}_2\text{O})_2$ and Uranophane $\text{Ca}(\text{UO}_2)_2(\text{SiO}_3\text{OH})_2 \cdot 5\text{H}_2\text{O}$. *Environmental science technology*, 45(6), 2510-2515.
55. Utsunomiya, S., Wang, L. M., Douglas, M., Clark, S. B., Ewing, R. C. (2003). The effect of ionizing radiation on uranophane. *American Mineralogist*, 88(1), 159-166.
56. Višňák, J., Sobek, L. (2016). Quantum chemical calculations and spectroscopic measurements of spectroscopic and thermodynamic properties of given uranyl complexes in aqueous solutions with possible environmental and industrial applications. In *EPJ Web of Conferences* (Vol. 128, p. 02002). EDP Sciences. 10.1051/epjconf/201612802002
57. Viswanathan, K., Harneit, O. (1986). Refined crystal structure of beta-uranophane, $\text{Ca}(\text{UO}_2)_2(\text{SiO}_3\text{OH})_2 \cdot 5\text{H}_2\text{O}$. *American Mineralogist*, 71(11-12), 1489-1493.
58. Wall, N. A., Clark, S. B., McHale, J. L. (2010). Synthesis and characterization of 1: 1 layered uranyl silicate mineral phases. *Chemical Geology*, 274(3-4), 149-157.
59. Wang, Z., Zachara, J. M., Gassman, P. L., Liu, C., Qafoku, O., Yantasee, W., Catalano, J. G. (2005). Fluorescence spectroscopy of U (VI)-silicates and U (VI)-contaminated Hanford sediment. *Geochimica et Cosmochimica Acta*, 69(6), 1391-1403. DOI:10.1016/j.gca.2004.08.028.
60. Wronkiewicz, D. J., Bates, J. K., Wolf, S. F., Buck, E. C. (1996). Ten-year results from unsaturated drip tests with UO_2 at 90 C: implications for the corrosion of spent nuclear fuel. *Journal of Nuclear Materials*, 238(1), 78-95.

Figures

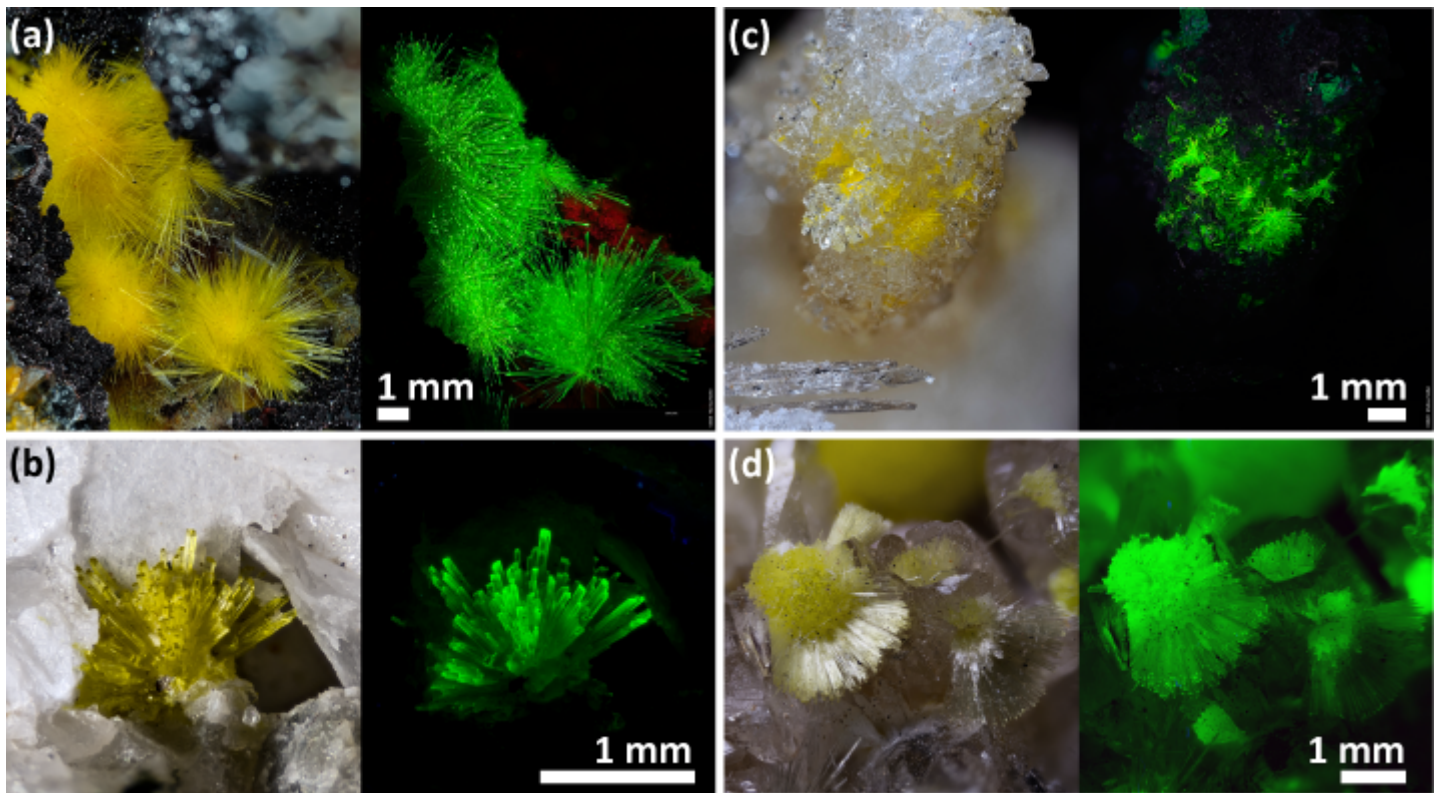


Figure 1

Photographs of specimens of the investigated minerals, each under white light (left) and 365 nm excitation (right). (a) Uranophane-a (Menzenschwand, Baden-Württemberg, Germany); (b) uranophane-b (Pasel adit, Radhausberg, Bad Gastein, Austria); (c) sklodowskite (Paliokamariza Mines, Lavrion Mining District, Greece); (d) haiweeite (Perus, São Paulo, Brazil). Scale bar is 1 mm in each case. *Photographs: (a), (c) M. Noller 2020, (b), (d) M. Stark 2021*

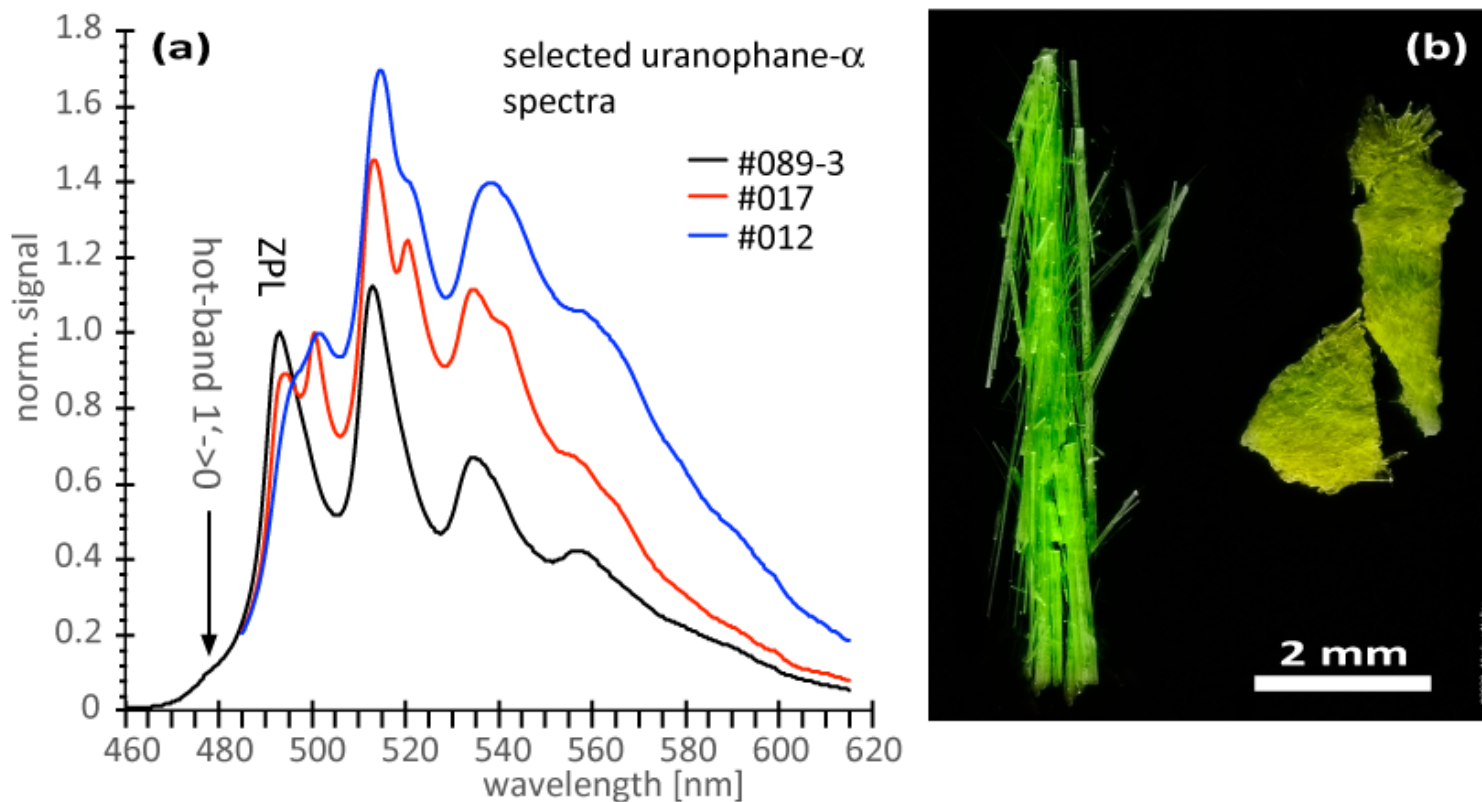


Figure 2

Obviously different: (a) Spectra of three samples of uranophane- α , for each of them identity has been confirmed by XRD and EDS. For #089-3 (black; Musonoi, DR Congo), the zero-phonon line (ZPL) is pronounced as compared to #017 (red; Rauris, Austria) and #012 (blue; Le Limouzat, France). In #089-3, no double-peak structure is visible, while it is obvious in #017, which resembles the spectrum given in (Kuta, 2013). In spectrum #012, structure is already partially lost. (b) This photograph (image width 8 mm) of two uranophane- α aggregates extracted from different samples from Menzenschwand, Germany, exemplifies the emission color-range from green (left) to yellow (right). Both samples were imaged together under 365 nm illumination

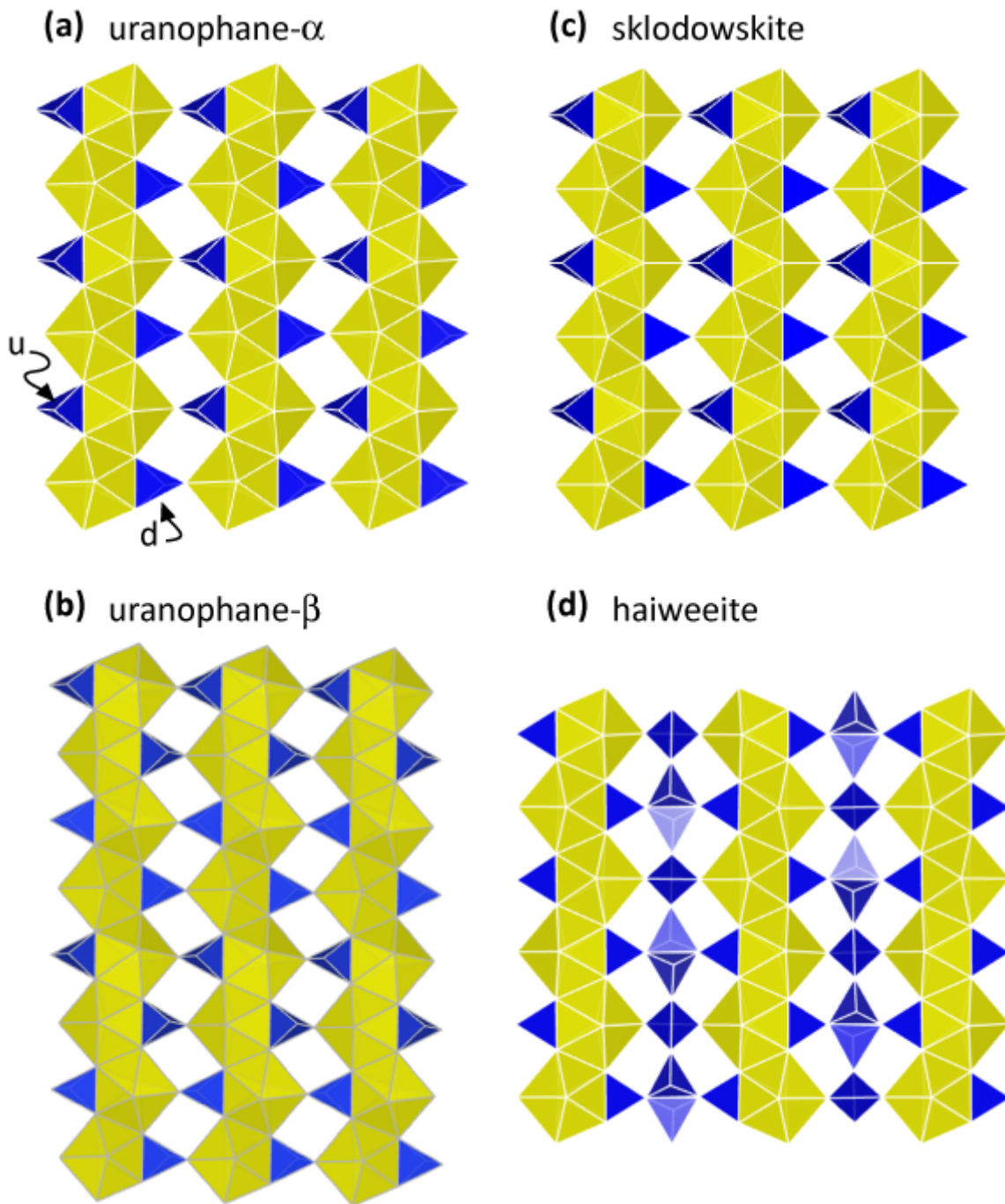


Figure 3

Similarities and differences in the structures of (a) uranophane-a (Barinova et al. 2001), (b) uranophane-b (Barinova et al. 2003), (c) sklodowskite (Mokeyeva 1964) and (c) haiweeite (Plášil et al. 2013). For direct comparison of relevant structural elements of the four minerals, only the sheets are depicted, composed by chains of (UO_7) -pentagonal bipyramids (yellow) with attached (SiO_4) -tetrahedra (blue). Other structural elements (like cations, or water molecules) are omitted for clarity. Up (*u*) and down (*d*) oriented SiO_4 -tetrahedra are highlighted. While uranophane-a and sklodowskite base on a *..udud..* motif, the different building motif *..uudduudd..* of uranophane-b is clearly visible. Haiweeite shows more complex building units. Visualization of structures with VESTA (Momma and Izumi 2011)

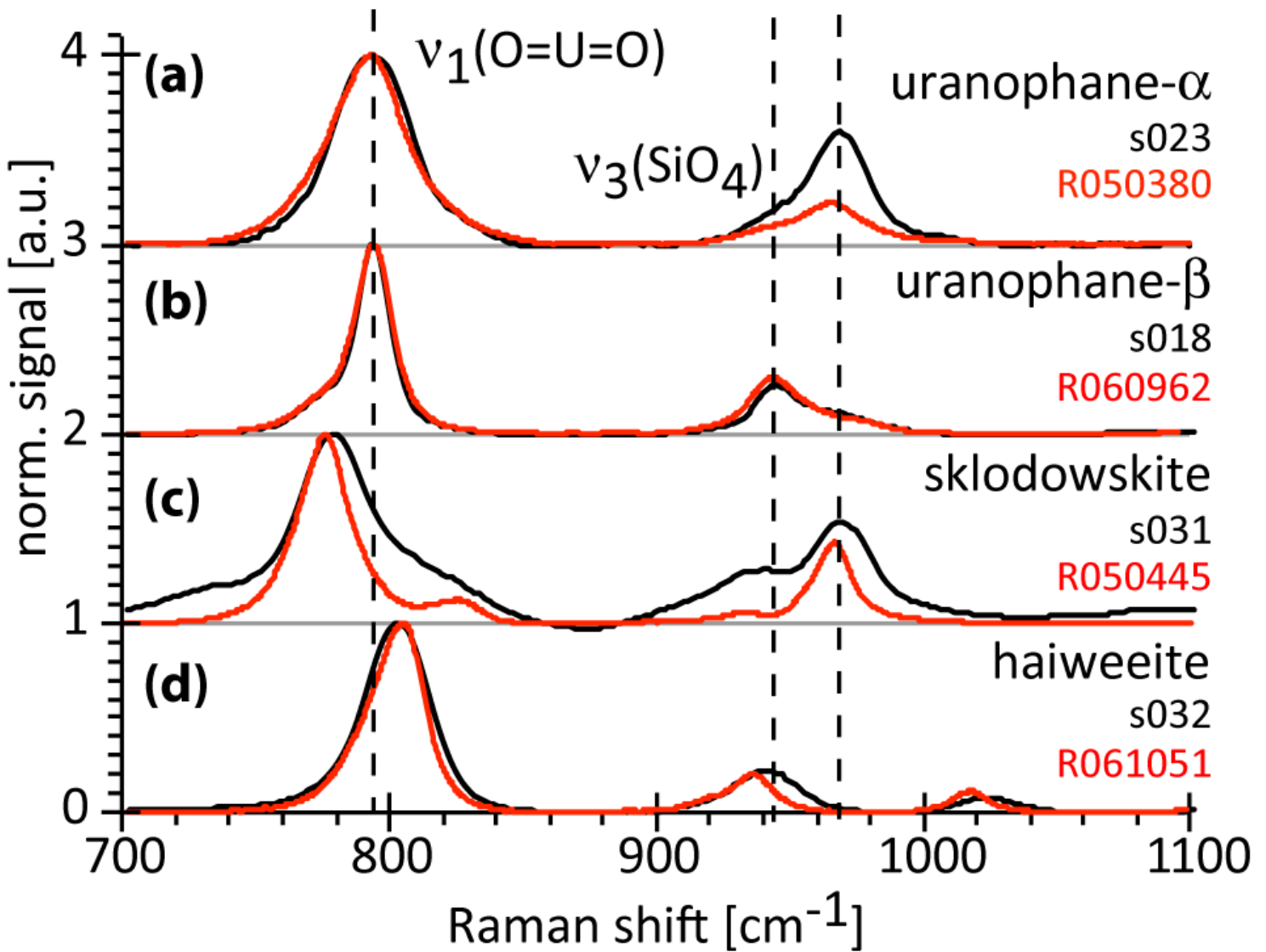


Figure 4

Raman spectra of the four minerals in the discriminating range of 700 cm^{-1} to 1100 cm^{-1} . Measured data (black) is shown together with reference data (red) taken from the RRUFF-project (ruff.info): (a) uranophane-a, (b) uranophane-b, (c) sklodowskite and (d) haiweeite. The Raman peak around 800 cm^{-1} is associated with the linear stretching vibrations of $(\text{UO}_2)^{2+}$ and converts into the phononic energy difference of the luminescence spectra. Notably, this energy is the same for uranophane-a and uranophane-b. Bands around 950 cm^{-1} relate to vibrations of SiO_4 -tetrahedra and are distinctive for the four species

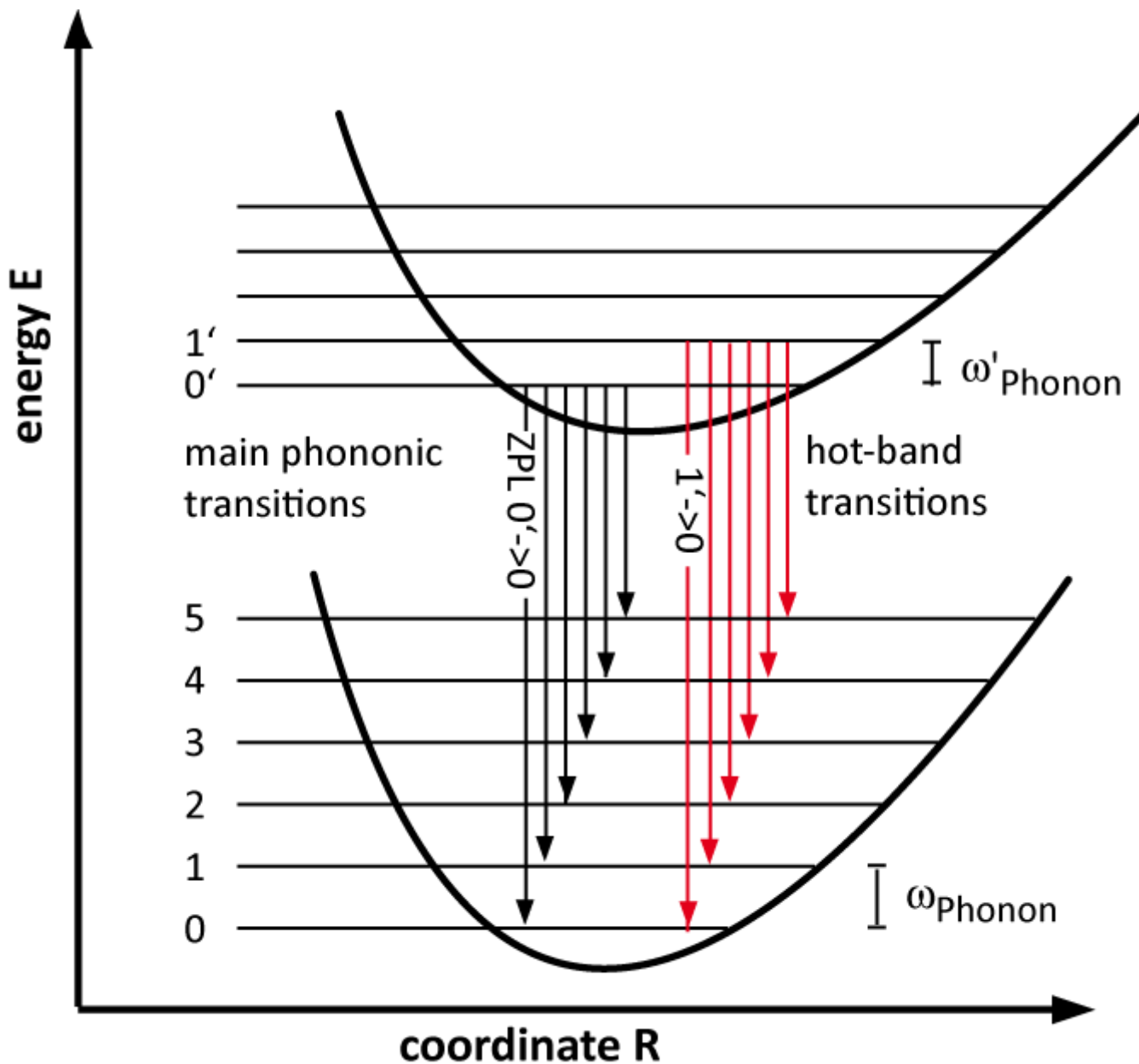


Figure 5

Scheme illustrating relevant electronic ground- and excited state together with the phononic levels of the uranyl-ion (Drobot, 2015a; Višňák and Sobek 2016). The system relaxes from the bottom of the excited state to one of the phononic levels of the ground state (black), resulting in the main phononic bands in the luminescence spectrum, with phonon energy ω_{phonon} equivalent to the $(\text{UO}_2)^{2+}$ stretching vibrations. The zero-phonon line (ZPL), denoted $0' \rightarrow 0$ is the transition without contribution of a phonon. Hot-band transitions (red) start at 1', the thermally excited state of the excited electronic state. Details see text

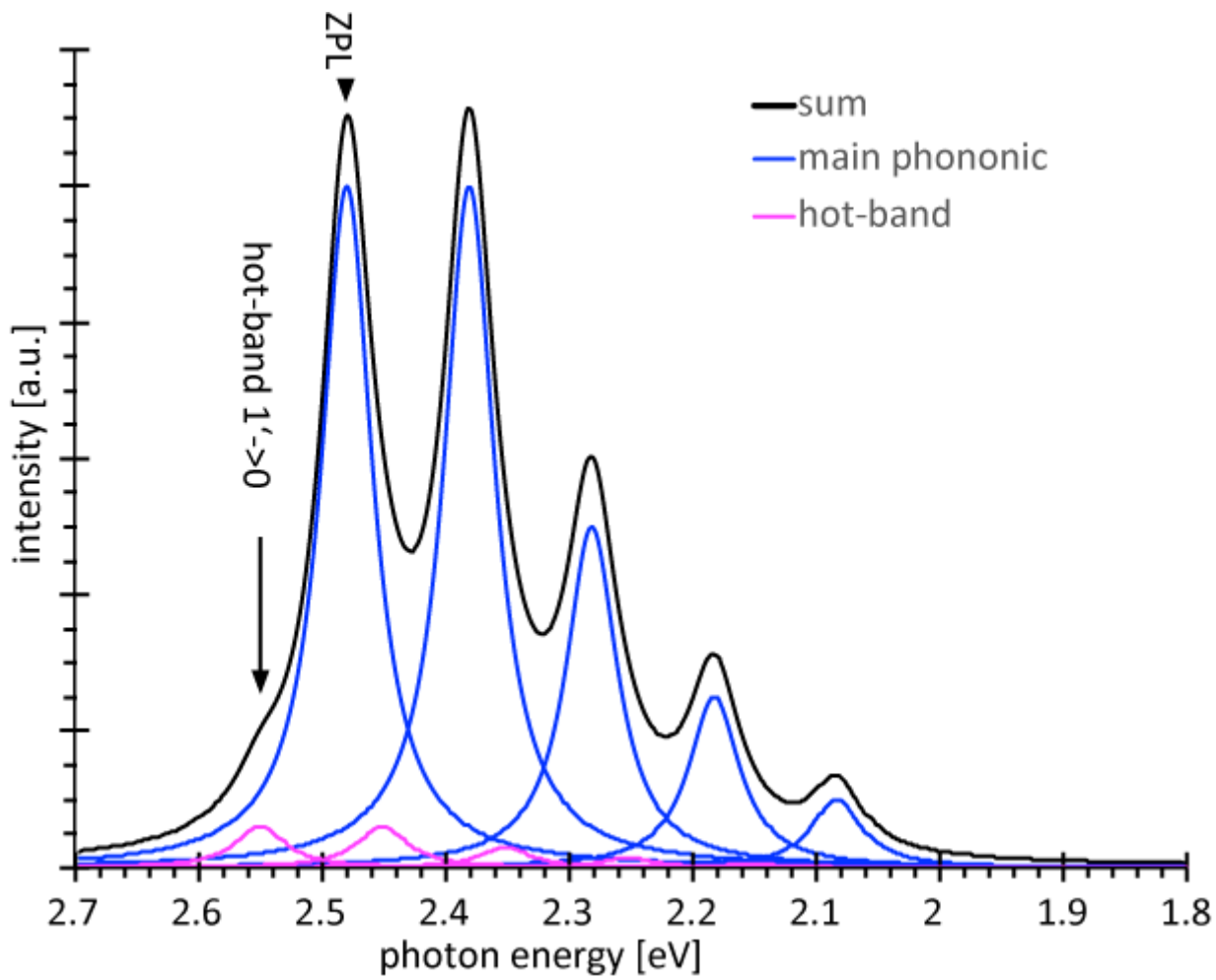


Figure 6

Generic spectrum (black) as model for uranyl-mineral luminescence, composed of dominant phononic (blue) and small hot band (pink) contributions (Drobot 2015a, Višňák and Sobek 2016). Details see text

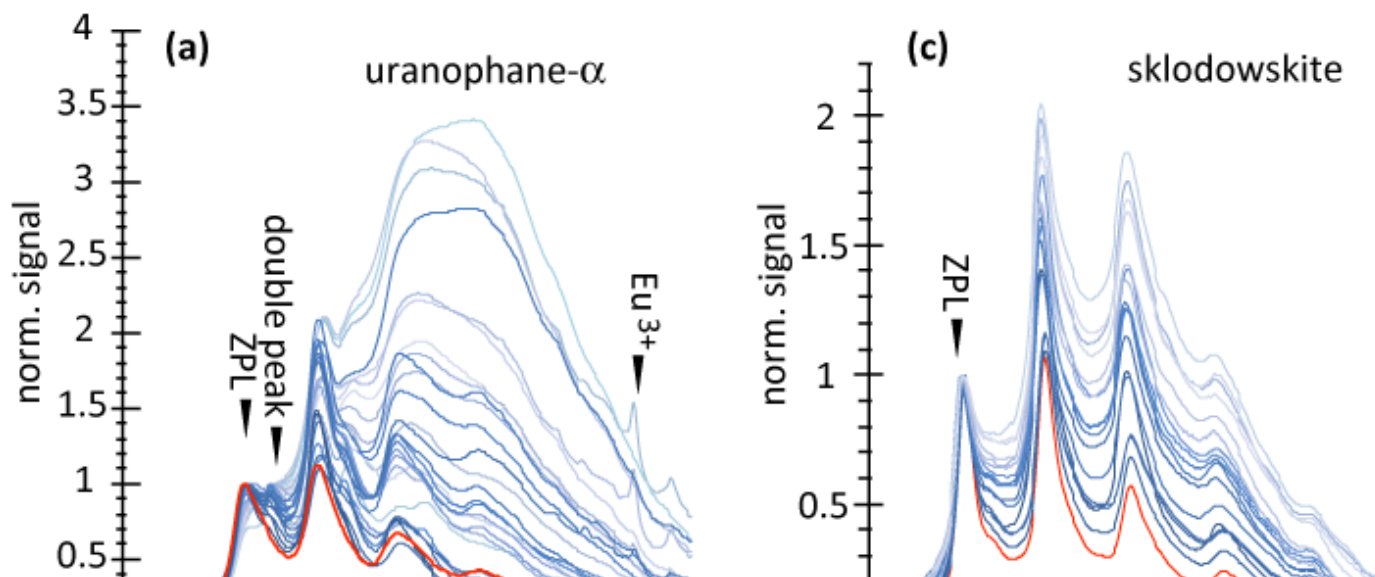


Figure 7

Ensembles of spectra (normalized to the zero-phonon line, ZPL) acquired on numerous samples of the four species: (a) uranophane- α , (b) uranophane- β , (c) sklodowskite and (d) haiweeite. The ZPL, the double peak structure and contributions of Eu^{3+} are marked. Large spectral variability with emerging double peak structure is evident in the case of uranophane- α . For each of the species the base spectrum is highlighted in red, details see text. Note, due to normalization to the ZPL, the spectra cannot directly be compared concerning their intensities

Figure 8

Measurement along the axis of an individual uranophane- α crystal (#086, Menzenschwand, Germany). Data have been taken every 25 μm . (a) In the series of spectra prominent variations of a double-peak structure are visible. To guide the eye, spectra taken at 0 μm , 250 μm , 500 μm and 750 μm are highlighted in red, data offset in the signal scale is 0.15 each. (b) The variability of the spectra along the crystal parameterized by the centroid wavelength $\lambda_{Uranophane} = \lambda_{Centroid}(493, \dots, 500.5\text{nm})$ (on x-axis) changing with position (y-axis)

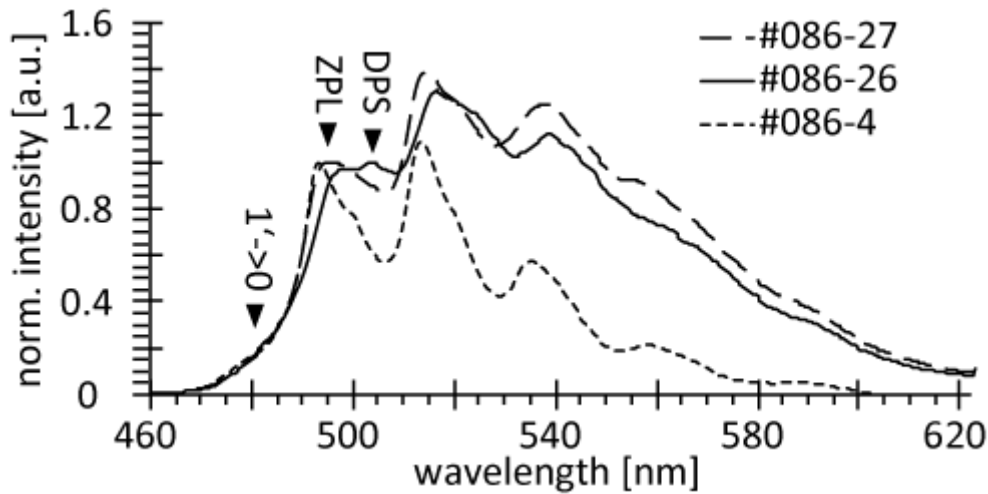


Figure 9

Three spectra of uranophane- α (extracted from the spectra scan, Fig. 8) highlight spectral variability within an individual crystal

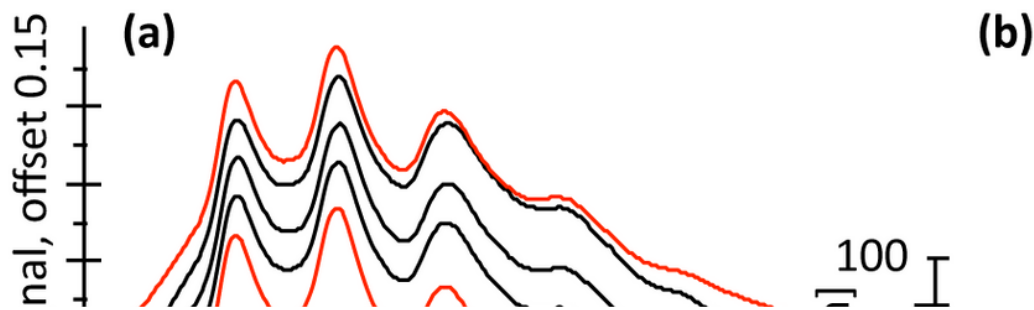


Figure 10

Measurement along the axis of an individual uranophane- β crystal (#088, Nopal mine, Mexico). Data have been taken every 25 μm . Unfortunately, crystals of uranophane- β were significantly smaller as compared to their counterpart uranophane- α , only 6 spectra could be taken. (a) The spectra of this series hardly vary in shape, no double peak structure is visible, which is consistent with the overall observation of Figure 7. To guide the eye, spectra taken at 0 μm and 100 μm are highlighted in red, data offset in the signal scale is 0.15 each. (b) The variability of the spectra along the crystal is parameterized by the centroid wavelength $\lambda_{\text{Uranophane}} = \lambda_{\text{Centroid}}$ (493,,,,,500.5nm) (on x-axis) changing with position (y-axis)

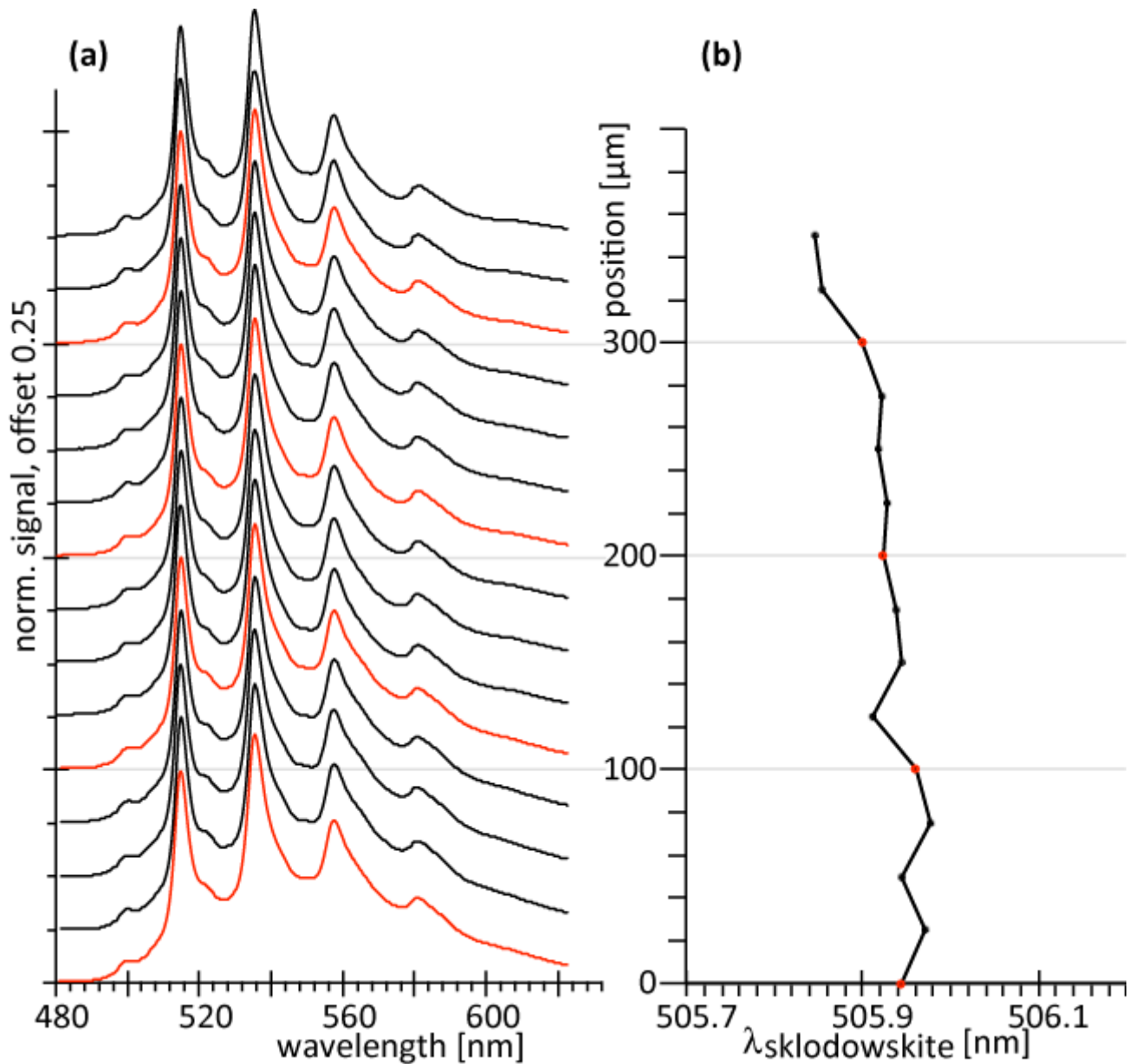


Figure 11

Measurement along the axis of an individual sklodowskite crystal (#090, Clara mine, Germany). Data have been taken every 25 μm . (a) The spectra are rather uniform over the whole length of the crystal; no double peak structure is visible. To guide the eye, spectra taken every 100 μm are highlighted in red, data offset in the signal scale is 0.25 each. (b) The variability of the spectra along the crystal is parameterized by the centroid wavelength $\lambda_{\text{Uranophane}} = \lambda_{\text{Centroid}}$ (503.....510nm)

Figure 12

Normalized base spectra, (a) uranophane- α (Menzenschwand, Baden-Württemberg, Germany), (b) uranophane- β (Pasel adit, Radhausberg, Bad Gastein, Austria), (c) sklodowskite (Clara mine, Oberwolfach, Germany) and (d) haiweeite (Los Azules mine, Atacama, Chile)

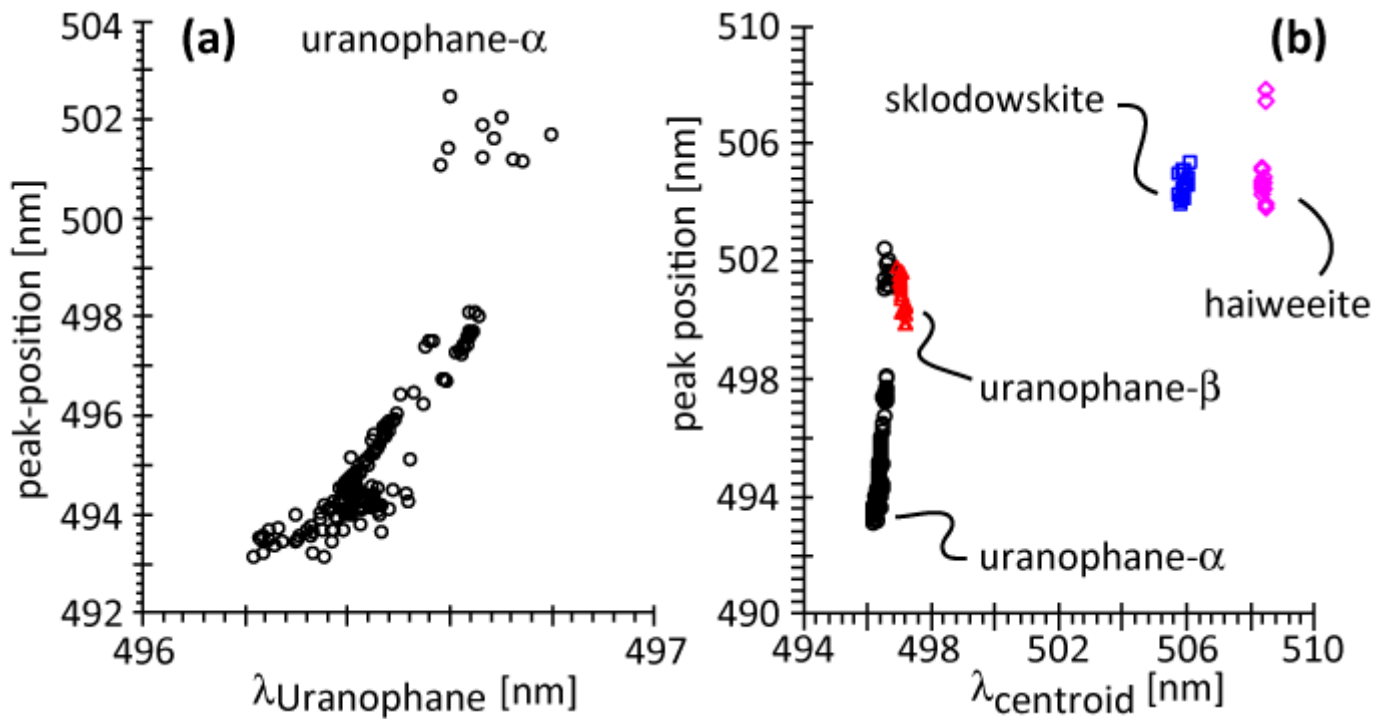


Figure 13

(a) Peak positions of the zero-phonon line (ZPL) of uranophane- α (on vertical axis) in dependence of the ordering parameter $\lambda_{\text{Uranophane}} = \lambda_{\text{Centroid}}$ (493.....500.5nm) (horizontal axis). Clearly, as spectra show increasing double peak contribution with higher values of $\lambda_{\text{Uranophane}}$ the ZPL shifts to longer wavelength. At around 496.7 nm, the ZPL starts to get drowned in the overall broadened structure, with the emerging second peak dominating (around 501 nm). (b) Comparison of the variation of ZPL-position with the respective ordering parameter $\lambda_{\text{Centroid}}$ for the four species uranophane- α (black circles), uranophane- β (red triangles), sklodowskite (blue squares) and haiweeite (magenta diamonds). The part of the uranophane- α data (black) at around $\lambda_{\text{Uranophane}} > 496.66\text{nm}$ and 502 nm peak position

represents spectra where the ZPL is no longer discernable. It partially overlaps with the ensemble of uranophane- β (red). Compared to uranophane- α ZPL-shift is small in the other cases. Details see text

Figure 14

Reconstruction of three spectra based on the assumption of phononic- and hot-band contributions (Drobot 2015a, Višňák and Sobek 2016): (a) uranophane-b, #117-6, (b) uranophane- α , #086-4 and (c) uranophane- α , #065. While the reconstruction of uranophane-b is possible under the assumption of small hot-band contributions, this is not evident for uranophane- α due to a marked double peak structure. However, assuming uranophane-b to contribute spectrally, reconstruction of the measured uranophane- α spectra becomes possible at small hot-band contributions. In cases (b) and (c), hot-band contributions are kept at the same level as in (a), while a significant contribution of uranophane-b spectrum is added. Notably, hot-bands of uranophane- α coincide with main phononic bands of uranophane-b. In all figures, measured data are given in black, main phononic contributions in blue, intrinsic hot-bands in magenta and scaled uranophane-b contributions as dashed brown lines. In each case, the sum spectrum is given in red. Details see text